

Shape-Independent Fluidization in Epithelial Cell Monolayers

Pradip K. Bera¹, Anh Q. Nguyen^{2,3}, Molly McCord^{1,4}, Dapeng Bi^{2,3}, Jacob Notbohm^{1,4,†}

¹ Department of Mechanical Engineering, University of Wisconsin–Madison, Madison, WI, USA

² Department of Physics, Northeastern University, Boston, MA, USA

³ Center for Theoretical Biological Physics, Northeastern University, Boston, MA, USA

⁴ Biophysics Program, University of Wisconsin–Madison, Madison, WI, USA

† Correspondence: jknotbohm@wisc.edu

Abstract

Tissue fluidity regulates many critical biological processes, including embryonic development, wound healing, and cancer metastasis. In confluent epithelia, where cell packing fraction is effectively fixed, the prevailing paradigm postulates that transitions between solid-like jammed and fluid-like unjammed states are governed by a geometric cell shape index determined by the balance of cortical tension and intercellular adhesion. Here, we challenge this geometric framework by reporting a mode of fluidization in epithelial monolayers that is entirely shape-independent. We observe that reducing cell-cell adhesion triggers a substantial increase in fluidity, yet this occurs without any corresponding change in cell shape, cell density, substrate traction, or junctional line tension. This decoupling of shape and fluidity reveals that current vertex models, which treat adhesion solely as a contribution to interfacial tension, are incomplete. To reconcile these findings, we extend the theoretical framework to account for the dual nature of adhesion—its thermodynamic role in setting interfacial adhesion energy at the cell-cell junctions and its kinetic role in generating viscous drag as cells slide past their neighbors. This generalized model quantitatively captures the experimental data, demonstrating that the interplay between adhesive energetics and dissipative friction is essential for a complete understanding of epithelial fluidity.

Introduction

The ability of a tissue to deform and flow—referred to as tissue fluidity—underpins essential biological processes such as morphogenesis, wound healing, and cancer invasion [1–4]. In epithelial monolayers, tissue fluidity is commonly framed as a collective mechanical property that emerges from cell-scale geometry and can control transitions between a jammed, solid-like state, wherein neighbor exchanges are suppressed, and an unjammed, fluid-like state, wherein cells can readily rearrange [5–7]. Tissue fluidity promotes wound healing in live *Drosophila* wing imaginal discs [8] and mouse skin epidermis [9]. Given its central role in shaping tissue architecture and function, identifying the mechanisms that regulate fluidity is a fundamental question in tissue mechanics.

Current understanding is that tissue fluidity is controlled primarily by a cell shape index q , defined as the ratio of perimeter to square root of area of each cell. When the average shape index is above a critical value, $q_c \approx 3.8$, tissues are expected to transition from solid-like to fluid-like behavior [10, 11]. Physically, cell shape determines the geometric compatibility of cells within a confluent monolayer, where each cell tends to maintain its preferred, homeostatic area and perimeter. In this setting, the shape index quantifies how easily these constraints can be satisfied collectively. Cells with a higher shape index are more elongated and possess greater geometric freedom: they can undergo shape fluctuations and small deformations without substantially changing their area or perimeter. This makes them mechanically more compliant, leading to

a fluid-like state. In contrast, rounded cells (with a lower shape index) are geometrically constrained. Any deformation typically requires a significant change in perimeter or area, which incurs an energetic penalty, leading to a rigid, solid-like response. Consequently, cell shape directly influences the energetic barrier to deformation and neighbor exchange [12]. Experimental observations across diverse epithelial systems are broadly consistent with this picture: tissues composed of more elongated cells, characterized by a higher shape index, often exhibit enhanced motility, frequent neighbor exchanges, and collective flows [13–19]. These findings seem to position cell shape index q as a unifying order parameter for epithelial fluidity.

While the relationship between cell shape and tissue state has been established phenomenologically, its predictive power relies on specific physical assumptions. In the quasistatic limit—wherein cells are jammed or nearly quiescent—shape is governed strictly by the balance of mechanical forces such as cortical tension, adhesion, and pressure [20–23]. Under these conditions, the tissue can be treated as a rate-independent system residing near an energy minimum, which is a fundamental premise of vertex-type models used to explain geometric-driven jamming. However, this framework breaks down when cellular motility and dynamics become appreciable. In such regimes, cell shape reflects only the underlying rate-independent mechanical constraints; the shape index cannot fully capture rate-dependent effects such as dissipative forces due to relative motion between cells. Hence, there is a need for approaches that go beyond the static energy landscape described by cell shape to explicitly account for the dynamics within the cell monolayer.

Here, we study collective migration within epithelial cell monolayers at constant number density and report a fluidization that is independent of cell shape. This surprising fluidization is caused by perturbing cell-cell adhesions, and we show that it is not caused by the line tension at the cell-cell interfaces nor the traction applied by the cells to the substrate. To explain how the adhesion-mediated fluidization can be independent of shape, we employ an extended vertex model that accounts for two effects of cell-cell adhesion, as follows. Firstly, adhesion is described physically by an interfacial surface energy, which describes the change in energy as cells adhere to one another. The interfacial surface energy is mathematically equivalent to adding a negative term to the effective junctional line tension, thereby acting against cortical contractility [24–30]. Hence, adhesion reduces line tension, which softens cells and lowers the energetic barriers to deformation and neighbor exchange, facilitating rearrangements within a confluent layer [31]. Secondly, adhesion generates viscous drag at cell-cell interfaces, introducing a resistance that penalizes relative motion between adjacent cells [30, 32–35]. Cell-cell adhesion, therefore, contributes to the physics in two ways, which we refer to, respectively, as an *energetic* contribution and a *dissipative* contribution. Our extended vertex model accounts for both the energetic and dissipative contributions of adhesions, and it captures the experimental observations, namely the dissipative contribution of cell-cell adhesion enables shape-independent excursions in the rigidity phase diagram that are inaccessible in purely geometric descriptions.

Results

Blocking E-cadherin-based cell-cell adhesion fluidizes cell monolayers without altering cell shape

Here, we aim to quantify tissue fluidity in confined monolayers of constant size. We seeded micropatterned islands of Madin-Darby canine kidney (MDCK) type II cells, approximately 1 mm in diameter, on polyacrylamide substrates with a Young’s modulus of 6 kPa (Fig. 1a), following established protocols [36, 37]. To maintain a constant cell density, n , in the range of $2500 < n < 3200 \text{ mm}^{-2}$ during our experiments, cell proliferation was inhibited using mitomycin C [38] after the desired density was reached (Supplementary Fig. 1). Cell-cell adhesion was disrupted by briefly exposing the monolayers to calcium- and magnesium-free phosphate-buffered saline (PBS). Subsequently, the reformation of adherens junctions was inhibited partially by adding the function-blocking antibody DECMA-1, which binds to E-cadherin

and stabilizes it in a monomeric state, hence blocking E-cadherin-based cell-cell adhesion (Supplementary Fig. 2) [19, 35, 39, 40]. We define the experiment time $t = 0$ h as the time of DECMA-1 addition. Cell nuclei were tracked in two dimensions using time-lapse microscopy, enabled by the expression of green fluorescent protein fused to a nuclear localization signal (Fig. 1b).

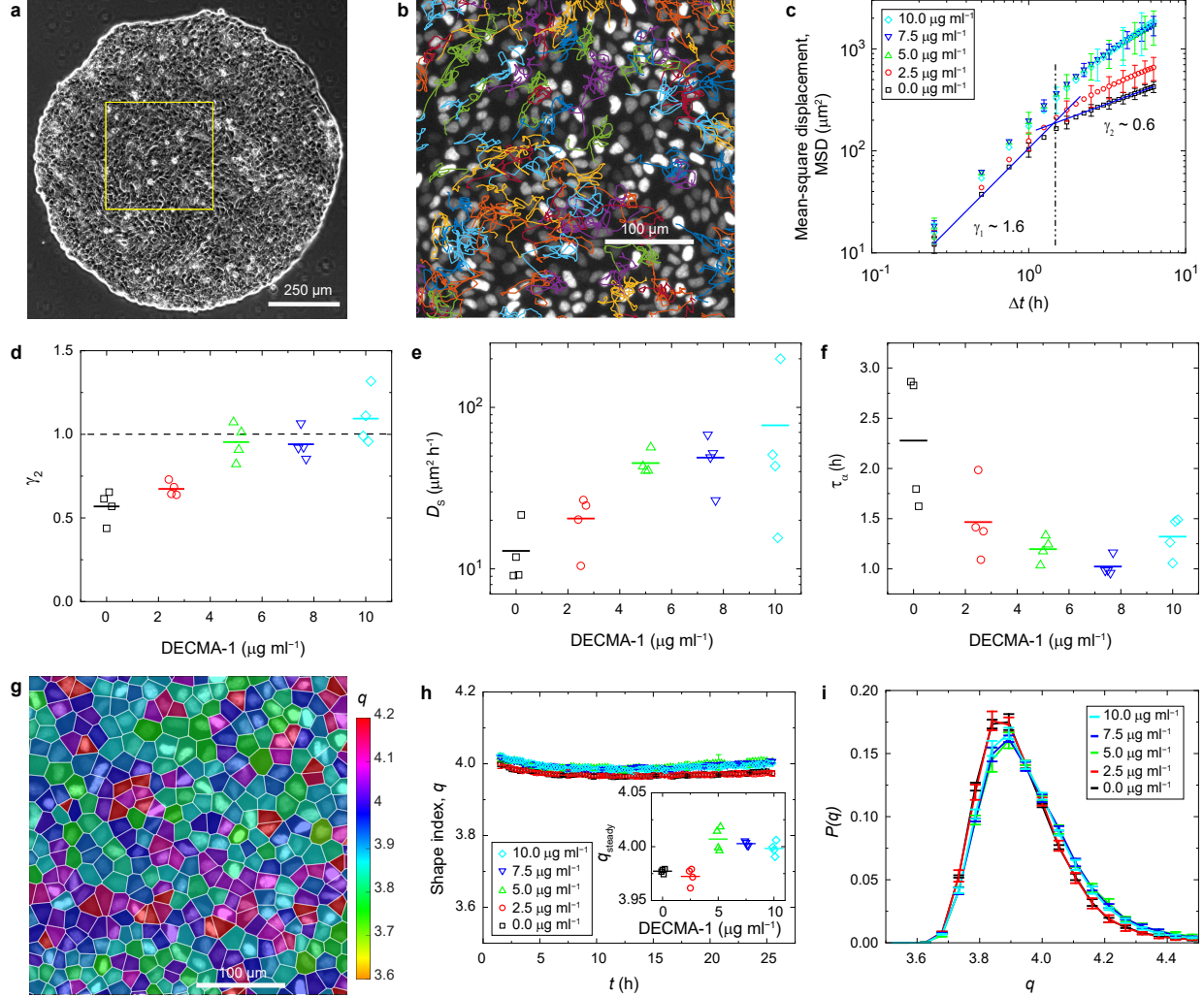


Figure 1: Fluidity of MDCK cell layers treated with the anti-E-cadherin antibody DECMA-1. (a) Phase-contrast image of a cell island, with the yellow boxed region magnified in later panels. (b) Representative trajectories overlaid on the nuclei image and color-coded to distinguish between different trajectories. (c) Mean-square displacement (MSD) calculated from steady-state trajectories ($t = 4$ h to 24 h) for each DECMA-1 concentration. Blue lines show fits to the $0 \mu\text{g ml}^{-1}$ DECMA-1 condition over the Δt (lag time) ranges $0.25\text{--}1.0$ h and $2.5\text{--}6.25$ h, yielding MSD exponents γ_1 and γ_2 , respectively. Fits were extrapolated to estimate the superdiffusive-subdiffusive crossover time $\Delta t_c \approx 1.5$ h, and length scale, $L_c \approx 17 \mu\text{m}$. (d–f) Scatter plots for individual islands at different DECMA-1 concentrations showing (d) long-time MSD exponent, γ_2 , with dashed line indicating the subdiffusive boundary ($p = 8.5 \times 10^{-7}$), (e) self-diffusivity, D_s in semi-log scale ($p = 0.014$), (f) structural relaxation time (uncaging time), τ_α , extracted using DDM analysis ($p = 3.3 \times 10^{-3}$). (g) Image of cell nuclei overlaid with Voronoi tessellations, color-coded by the cell shape index, q . (h) Average q over time. Inset: steady-state shape index q_{steady} , defined as the average over $t = 23\text{--}24$ h ($p = 1.1 \times 10^{-3}$). (i) Probability distributions of steady-state shape index, $P(q)$. Error bars are standard deviations across different independent cell monolayers. In all scatter plots, markers indicate data from independent cell monolayers, and horizontal lines denote means of respective groups.

After reducing cell-cell adhesion, tissue fluidity was quantified using the mean-square displacement

(MSD) calculated from steady-state cell trajectories acquired between $t = 4$ h and 24 h (Fig. 1c). In untreated monolayers, the MSD exhibited a crossover from short-time superdiffusive dynamics, characterized by an exponent $\gamma_1 = 1.6$ (fitted over the lag time, Δt , in the range 0.25–1.0 h), to long-time subdiffusive dynamics with an exponent $\gamma_2 = 0.6$ (fitted range of Δt : 2.5–6.25 h). This crossover occurred at $\Delta t_c \approx 1.5$ h, corresponding to a characteristic length scale $L_c \approx 17$ μm . Notably, this length scale is comparable to the average cell diameter (≈ 20 μm), indicating that long-time dynamics are increasingly constrained by caging effects arising from neighboring cells. With increasing DECMA-1 concentration, the long-time MSD exponent increases and then saturates for concentrations above 5.0 $\mu\text{g ml}^{-1}$ (Fig. 1d). We also computed the long-time self-diffusivity D_s , defined as $D_s = \lim_{t \rightarrow \infty} \text{MSD}(\Delta t)/(4\Delta t)$, which increases by more than a factor of six due to DECMA-1 (Fig. 1e). These trends indicate that blocking E-cadherin-based cell-cell adhesions enhances tissue fluidity.

To further characterize the dynamics, we applied differential dynamic microscopy (DDM) [41] to the phase-contrast image sequences to extract the structural relaxation (uncaging) time τ_α (see Methods for details). Briefly, differential intensity patterns were computed in Fourier space at increasing time lags and azimuthally averaged, under the assumption of isotropic dynamics for each island. From these patterns, a time-dependent intermediate scattering function $F(k_0, \Delta t)$ was obtained using Eqn. 4 at a characteristic length scale $1/k_0 = 17$ μm , set by the MSD crossover due to neighbor caging (Supplementary Fig. 3). For each island, the uncaging time τ_α was defined as the $1/e$ decay time of the scattering function. Consistent with MSD-based measurements, τ_α decreased with increasing DECMA-1 concentration (Fig. 1f), providing further confirmation that blocking E-cadherin binding substantially enhances tissue fluidity.

To explain these observations, we first turned to the shape index q , defined as the ratio of perimeter to square root of area for each cell. Prior models, supported by experiments, have shown that higher fluidity within the tissue coincides with a greater shape index [7, 13, 15–19, 42–44]. To test whether shape index was elevated in response to reduced cell-cell adhesion, we quantified the average cell shape index q using Voronoi tessellations (Fig. 1g). Across all experiments, cells exhibited relatively high aspect ratios, yielding values of q well above the jamming transition threshold ($q_{\text{jamming}} = 3.81$), in agreement with previous studies [16]. Strikingly, despite the pronounced increase in tissue fluidity, reducing cell-cell adhesion did not produce a notable change in the cell shape index. Instead, the average shape index, q , barely increased for higher concentrations of DECMA-1 (Fig. 1h), and steady-state histograms of q showed nearly identical distributions (Fig. 1i).

To demonstrate that these results were not specific to the chosen cell density, we repeated these experiments in cell islands at a higher range of number density ($3500 < n < 4000$ mm^{-2}). Results were consistent: higher DECMA-1 concentrations led to higher fluidity in cell motion without any change in the cell shape index q (Supplementary Fig. 4).

DECMA-1 does not affect junctional line tension or traction forces

The observed change in fluidity with no change in shape index goes against the current paradigm in the field. To identify the underlying mechanism, we investigated the effects of the DECMA-1 treatment on the cellular forces. First, we considered the junctional line tension at each cell-cell interface. It is commonly suggested that cell-cell adhesions act as a negative line tension [21, 24, 25, 27–29], meaning that a reduction in adhesions by DECMA-1 would be expected to increase the junctional line tension. Alternatively, it is also possible that the effects of cell-cell adhesions are negligible compared to the cortical tension [29, 45, 46], in which case treatment with DECMA-1 would have no effect on the junctional line tension.

We probed junctional line tension using laser ablation experiments, wherein the junctions between neighboring cells were ablated, and the subsequent retraction rate was used as an indicator of the line ten-

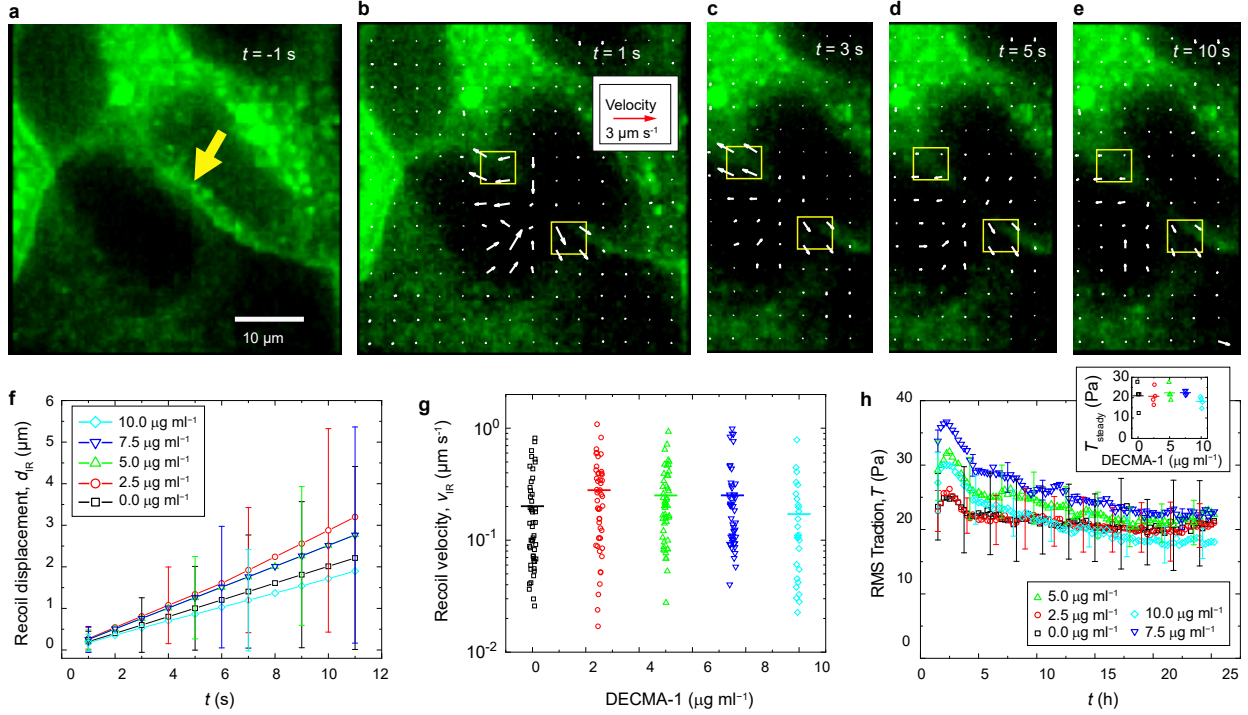


Figure 2: Effects of DECMA-1 on cell-cell interfacial adhesion energy and cell-substrate traction. (a) Representative confocal image of MDCK monolayers with a live stain for F-actin; the yellow arrow indicates the junction segment 1 s, before ablation. (b-e) The same region after ablation at successive time points. Overlaid velocity vectors were obtained from digital image correlation, and yellow boxes denote regions of interest at opposite ends of the ablation site. The scale bar shown in (a) is the same for all panels (a)-(e). (f) End-to-end recoil displacement d_{IR} as a function of time, averaged over 50 ablation sites for each DECMA-1 concentration. (g) Initial recoil velocity v_{IR} , a proxy for junctional line tension, computed over the first 8 s after ablation; horizontal lines denote means ($p = 0.55$; extended statistical test in Supplementary Table 1). (h) Root-mean-square (RMS) traction T as a function of time; inset: steady-state traction T_{steady} , defined as the average over $t = 23-24$ h ($p = 0.56$; extended statistical test in Supplementary Table 1). Error bars indicate standard deviations. Horizontal lines denote means of respective groups.

sion. Snapshots from a representative experiment are shown in Fig. 2a-e, wherein the cell edges on either side of an ablation recoiled over time. Under the assumption of constant viscosity, the short-time recoil velocity of the two ablated ends is proportional to the junctional line tension, whereas longer timescales reflect active remodeling processes. Hence, we quantified the recoil displacement over time (Fig. 2f), which in turn allowed us to calculate the initial recoil velocity at each DECMA-1 concentration (Fig. 2g). The initial recoil velocity v_{IR} spans nearly two orders of magnitude ($0.01-1 \mu\text{m s}^{-1}$), reflecting substantial mechanical heterogeneity within the monolayer. The relationship between DECMA-1 concentration and recoil velocity was not monotonic: the recoil velocity in response to $2.5 \mu\text{g ml}^{-1}$ DECMA-1 was slightly larger than the control, and the recoil velocities for all other concentrations were not statistically different from the control (Supplementary Table 1). This negligible change in line tension does not explain the substantial effects of DECMA-1 on tissue fluidity.

Next, we considered that in response to the DECMA-1 treatment, the cells may have altered their force production, which can have a strong effect on fluidity in this system [16]. Therefore, we quantified the traction over time using traction force microscopy (Supplementary Fig. 5) [47-49]. The root-mean-square (RMS) traction was nearly constant in time, and the steady state traction was not statistically different for different DECMA-1 concentrations (Fig. 2h), ruling out traction as the reason for the DECMA-1-induced fluidization. Hence, two of the major controllers of tissue fluidity and shape index identified in prior work, namely junctional line tension and traction [10, 13, 16, 17, 42], do not explain the observations presented

here.

Perturbing cell-cell adhesion by calcium chelation leads to shape-independent fluidization

To independently perturb cell-cell adhesion through a mechanism different from antibody-mediated blocking, we performed complementary experiments using ethylene glycol tetraacetic acid (EGTA). Cadherin-based cell-cell adhesion requires extracellular calcium ions [50]. EGTA chelates Ca^{2+} in the culture medium, thereby weakening cadherin-mediated cell-cell adhesion. At EGTA concentrations ≥ 2 mM, monolayers lost confluency and cells detached from the substrate; therefore, all measurements were restricted to concentrations ≤ 1.8 mM. Here, the 0 mM EGTA condition served as a sham control, and $t = 0$ h is the EGTA treatment time. We used a similar range of cell density as above ($2600 < n < 3300 \text{ mm}^{-2}$) (Supplementary Fig. 6).

Consistent with the DECMA-1 results, treatment with EGTA increases tissue fluidity, as evidenced by the increase in both the long-time MSD exponent γ_2 and the self-diffusivity D_s (Fig. 3a–c). Furthermore, the uncaging time τ_α decreased with increasing EGTA concentration, which also indicates that EGTA increases fluidity (Fig. 3d). Similar to the DECMA-1 treatment, distributions of shape index q were unchanged by EGTA, which again indicates a shape-independent fluidization (Fig. 3e, f). Also similar to DECMA-1, laser ablation experiments show that the junctional line tension did not change monotonically with EGTA concentration (Fig. 3g). Similar to the DECMA-1 experiments, the lower concentrations of EGTA (namely 0.5 and 1.0 mM) had retraction velocities that were statistically larger than control, but given the shape index q remained constant, these changes in line tension apparently had negligible effects. The EGTA treatment decreased the cell-substrate tractions, especially at the highest concentration of EGTA, for which the RMS traction decreased by nearly a factor of two (Fig. 3h, i). Interestingly, prior work using different treatments for cell force production showed that reducing traction causes a reduction in tissue fluidity [16]. The observation that fluidity was not reduced but rather increased in these experiments suggests that the effects of EGTA on the adhesions outweighed effects of traction.

Taken together, the EGTA experiments corroborate the DECMA-1 findings, demonstrating that weakening cell-cell adhesion enhances tissue fluidity without appreciably altering cell shape. Furthermore, even though EGTA also reduced traction, its effect on adhesions apparently outweighed effects of traction, indicating that cell-cell adhesions have an important contribution to fluidity.

An extended vertex model with dual roles of cell-cell adhesion captures shape-independent fluidity

To explain how the reduction of cell-cell adhesions increased tissue fluidity, we first describe how adhesions affect the tissue mechanics. As described above, there are two distinct yet interrelated mechanisms: an interfacial adhesion energy (energetic contribution) and a viscous drag (dissipative contribution). The energetic contribution is mathematically equivalent to a line tension, which is caused by two competing effects in epithelial cells. As illustrated in Fig. 4a, cortical tension tends to minimize cell perimeter by rounding the cell [27, 51]. Conversely, the presence of cell-cell adhesion at intercellular contacts anchors neighboring cortices together, promoting the elongation of cell-cell junctions [46, 52]. Energetically, therefore, the effect of cell-cell adhesion can reduce the junctional line tension [24–30], making cells softer and lowering the energetic cost of deformation and topological rearrangement, which effectively promotes tissue fluidity. The dissipative contribution is illustrated in Fig. 4b, wherein relative motion between neighboring cells stretches the adhesive bonds at their shared interface, placing them under tensile load. The continual formation, deformation, and rupture of these bonds resists relative sliding between cells and gives rise to an effective drag force localized at the cell-cell junction opposing intercellular motion, thereby dissipating mechanical energy. From a dynamical standpoint, adhesion impedes relative motion at the cell-cell junctions, imparting a viscous character to intercellular interactions [30, 32–35].

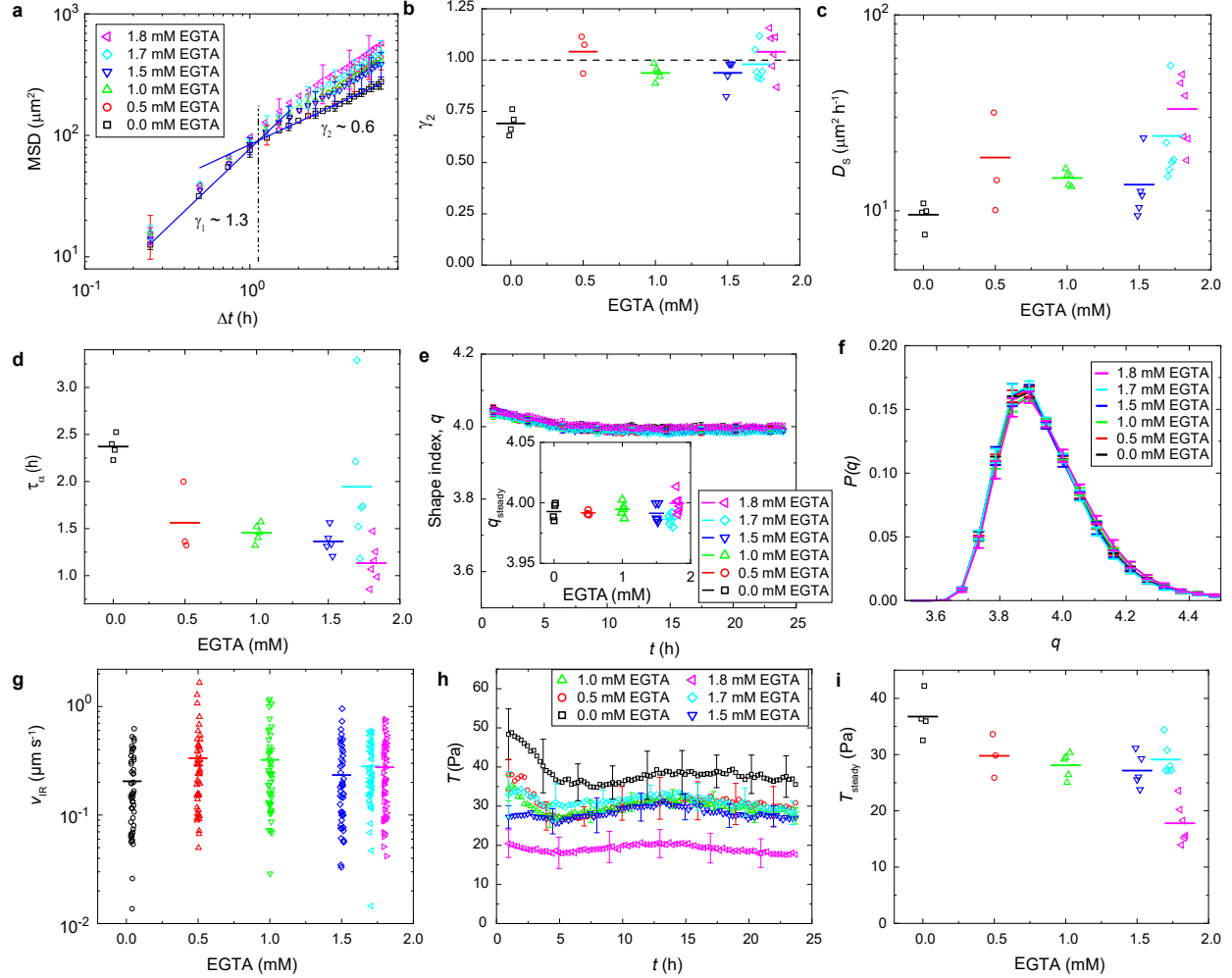


Figure 3: Effects of EGTA on tissue fluidization, cell shape, junctional line tension, and traction. (a) MSD calculated from steady-state trajectories ($t = 7\text{--}24$ h), for all EGTA conditions. Blue lines show fits to the 0 mM EGTA data in the Δt intervals 0.25–1.0 h and 2–6.25 h, with MSD exponents $\gamma_1 = 1.3$ and $\gamma_2 = 0.6$, respectively, yielding $\Delta t_c \approx 1.1$ h and $L_c \approx 10$ μm . (b–d) Scatter plots for each islands with EGTA showing (b) long-time MSD exponent, γ_2 ($p = 4.2 \times 10^{-4}$), (c) self-diffusivity, D_s ($p = 8.2 \times 10^{-3}$), and (d) uncaging time, τ_α ($p = 0.034$). (e) Average shape index, q , Inset: steady-state shape index q_{steady} , defined as the average over $t = 22\text{--}23$ h ($p = 0.86$; extended statistical test in Supplementary Table 2). (f) Steady-state distributions of q . (g) Initial recoil velocity, v_{IR} , measured after laser ablation; horizontal lines indicate mean ($p = 0.63$; extended statistical test in Supplementary Table 2). (h) RMS traction, T , reaching steady state after $t \approx 7$ h. (i) Steady-state traction, T_{steady} ($p = 2.1 \times 10^{-4}$). Error bars are standard deviations. In the scatter plots, markers indicate data from independent cell monolayers, and horizontal lines denote means of respective groups.

While the energetic contribution of cell-cell adhesion is implemented and studied extensively in the vertex model framework [8, 10, 42, 53–56], the dissipative aspect has received much less attention [57, 58]. Further, the effect of competition between the two aspects of cell-cell adhesion has not been studied to date. In the vertex model, cells follow the overdamped equation of motion $0 = \mathbf{F}_i^{\text{c-s}} + \mathbf{F}_i^{\text{int}} + \mathbf{F}_i^{\text{act}}$, where $\mathbf{F}_i^{\text{c-s}} = -\mu \dot{\mathbf{r}}_i$ is the viscous force between cell i and the substrate, with μ being the cell-substrate viscous coefficient, \mathbf{r}_i being the position of cell i , and the over-dot denoting a time derivative. $\mathbf{F}_i^{\text{int}} = -\nabla_{\mathbf{r}_i} E$ is the interaction force between cells arising from the tissue total energy function $E = \sum_i [K_A (A_i - A_0)^2 + K_P (P_i - P_0)^2]$, with K_A and K_P being the elastic moduli associated with area and perimeter deformations, respectively; A_i and P_i denote the instantaneous area and perimeter of cell i ; and A_0 and P_0 are the corresponding preferred values, which are material properties set by cellular physiology. $\mathbf{F}_i^{\text{act}} = \mu v_0 \hat{\mathbf{n}}_i$ is the active propulsion force produced by the

cell with magnitude v_0 and polarity $\hat{\mathbf{n}}_i = (\cos \theta_i, \sin \theta_i)$. The polarity angle θ undergoes rotational diffusion with zero mean and variance $2D_r$. The model can be made dimensionless using $\sqrt{\bar{A}}$ as the unit of length (with \bar{A} being the average cell area), $\mu/(K_A \bar{A})$ as the unit of time, and $K_A \bar{A}^{3/2}$ as the unit of force. Note, after rescaling dimensional variables x with these units, we use the nomenclature \tilde{x} to indicate the corresponding dimensionless form. All model calculations are performed using dimensionless variables (see Methods for parameter estimation).

Using the original vertex model described above, we first sought to reproduce the experimentally observed relationship between the self-diffusivity D_s and the cell shape index q . We ran simulations over a range of values of the dimensionless preferred perimeter $p_0 = P_0/\sqrt{A_0}$ (with $A_0/\bar{A} = 1$) and motility strength $\tilde{v}_0 = v_0\mu/(K_A \bar{A}^{3/2})$, while keeping all other parameters fixed. For each simulation, the mean shape index was computed as $q = \langle P_i/\sqrt{A_i} \rangle$ with the brackets indicating a mean over all cells. Additionally, the self-diffusivity D_s was measured in the simulations, allowing us to plot normalized D_s as a function of q for comparison to the experiments. Over the experimentally observed range of q , the experimental D_s increased sixfold (Fig. 4c). In contrast, the original vertex model produces only a weak increase in D_s across the experimentally observed q range, with a maximum change of just 1.2-fold, which occurred for an intermediate value of \tilde{v}_0 . This large quantitative mismatch demonstrates that the experimentally observed fluidization cannot be explained within the existing vertex model framework, in which changes in tissue dynamics are tightly constrained by changes in cell shape.

Motivated by the large changes in collective tissue fluidity that occur without appreciable changes in cell shape, we extend the original vertex model to explicitly incorporate both energetic and dissipative contributions of cell-cell adhesion, leading to a modified overdamped equation of motion,

$$0 = \mathbf{F}_i^{\text{c-s}} + \mathbf{F}_i^{\text{int}} + \mathbf{F}_i^{\text{act}} + \mathbf{F}_i^{\text{c-c}}. \quad (1)$$

Here, $\mathbf{F}^{\text{c-c}}$ is the drag force due to cell-cell adhesion and has the form [59]

$$\mathbf{F}_i^{\text{c-c}} = - \sum_{j \in S_i} \eta (\mathbf{r}_{ij} \cdot \hat{\mathbf{r}}_{ij}) \hat{\mathbf{r}}_{ij}, \quad (2)$$

where η is the junctional drag coefficient, S_i is the set of neighboring vertices of vertex i , $\mathbf{r}_{ij} = \mathbf{r}_i - \mathbf{r}_j$ denotes the edge vector from vertex j to vertex i , and $\hat{\mathbf{r}}_{ij} = \mathbf{r}_{ij}/|\mathbf{r}_{ij}|$ is the unit vector pointing from vertex j to vertex i . This yields the following dimensionless equation of motion:

$$\dot{\tilde{\mathbf{r}}}_i + \tilde{\eta} \sum_{j \in S_i} [(\tilde{\mathbf{r}}_{ij} \cdot \hat{\tilde{\mathbf{r}}}_{ij}) \hat{\tilde{\mathbf{r}}}_{ij}] = \tilde{\mathbf{F}}_i^{\text{int}} + \tilde{v}_0 \hat{\mathbf{n}}_i, \quad (3)$$

where $\tilde{\eta} = \eta \sqrt{\bar{A}}/\mu$ is the dimensionless junctional drag coefficient, and $\tilde{\mathbf{F}}_i^{\text{int}} = \mathbf{F}_i^{\text{int}}/(K_A \bar{A}^{3/2})$ is the dimensionless interaction force. In this extended vertex model, cell-cell adhesion controls two key parameters, p_0 and $\tilde{\eta}$, meaning that adhesion governs tissue fluidity by two competing mechanisms, namely the energetic and dissipative contributions described above. Interestingly, these two effects are in competition as follows. First, a reduction in adhesions would increase line tension (*i.e.*, decrease p_0), which reduces fluidity. Secondly, reducing adhesion would reduce adhesive drag (*i.e.*, reduce $\tilde{\eta}$), which enhances fluidity. As a result, tissue fluidity is no longer governed solely by geometric constraints but instead emerges from the interplay between energetic and dissipative contributions of cell-cell adhesion.

To enable quantitative comparison between simulations and experiments, we focus on two complementary observables: the self-diffusivity D_s and the dimensionless shape index q . The shape index q provides a direct and scale-independent measure of tissue structure and can therefore be straightforwardly compared between experiments and simulations. In contrast, self-diffusivity was normalized using the scales for length

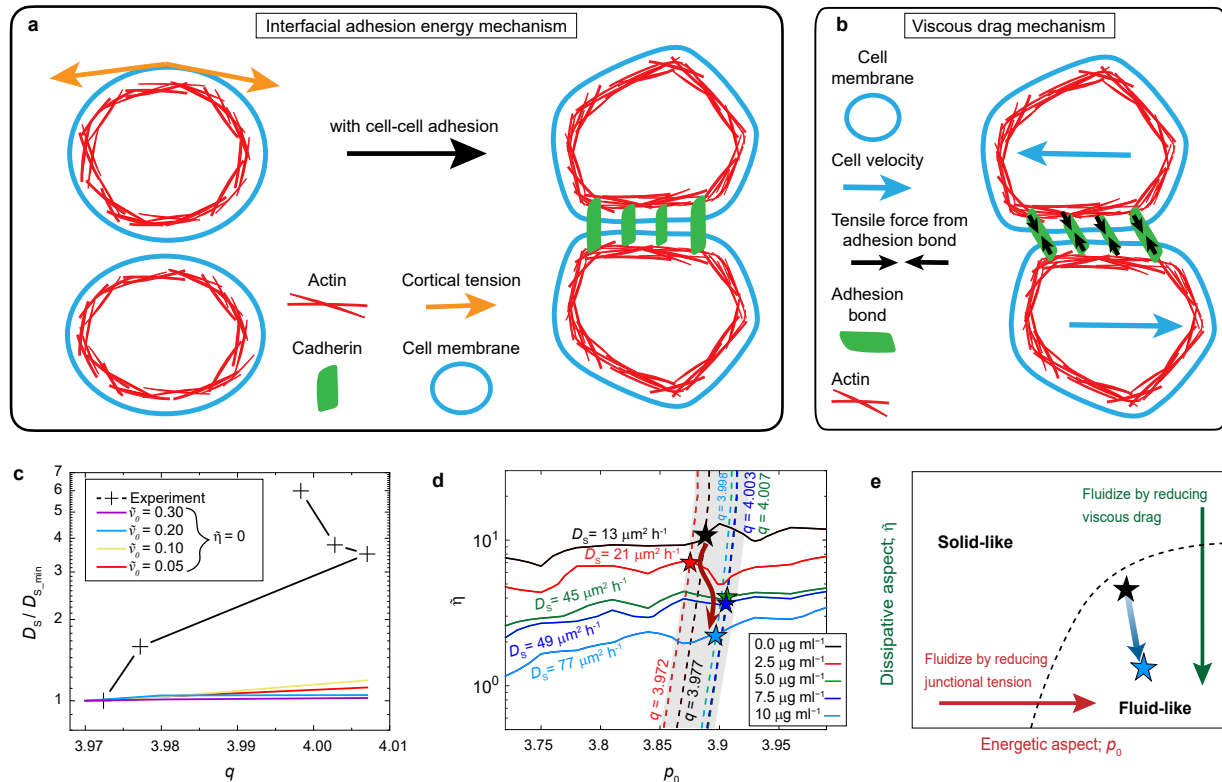


Figure 4: Mapping shape-dependent fluidization in epithelial monolayers onto vertex-model frameworks. (a) Schematic of the tension-related energetic contribution of cell-cell adhesion. Contractile tension generated by the actomyosin cortex tends to minimize cell perimeter and promote cell rounding, thereby disfavoring extended intercellular contacts. In contrast, cadherin-mediated adhesive interactions stabilize and extend cell-cell junctions, effectively reducing the junctional line tension and softening cells. (b) Schematic of the dissipative (drag-related) contribution of cell-cell adhesion, whereby adhesive bonds resist relative motion between neighboring cells and introduce viscous dissipation at cell-cell interfaces. (c) Self-diffusivity D_s (normalized to its lowest measured value) as a function of shape index q , as observed in experiments and using the original vertex model for different values of \tilde{v}_0 . The discrepancy between the curves from experiments and simulations demonstrates that the original vertex model does not capture the experimental observations. (d) Contours in the $(p_0, \tilde{\eta})$ parameter space of the extended vertex model for self-diffusivity D_s (using mean values from Fig. 1e) and cell shape index q (using mean values from Fig. 1h, inset). The background shading indicates experimental uncertainty in q (defined as the standard deviation of q across different cell monolayers). The intersections of the contours show the shape-independent trajectory through the $(p_0, \tilde{\eta})$ plane in response to DECMA-1-induced perturbations of cell-cell adhesion, as indicated by the brown arrow. (e) Conceptual phase diagram of tissue fluidity as a function of the energetic and dissipative components of cell-cell adhesion.

and time described above (see Methods for details on parameter estimation and Supplementary Table 3 for a summary of model parameters that best match the experiments).

Because our primary objective is to elucidate how cell-cell adhesion regulates tissue fluidity, we construct contour maps of both the dynamics (as quantified by the self-diffusivity D_s) and shape index q , for which the two independent contributions of adhesion serve as control variables. Specifically, the dissipative (drag-related) component of cell-cell adhesion, quantified by the dimensionless parameter $\tilde{\eta}$, is used as one axis, while the energetic (tension-related) component, quantified by the preferred shape index p_0 , is used as the other axis. These contour maps enable us to disentangle and assess the relative contributions of the energetic and dissipative aspects of cell-cell adhesion on tissue fluidity. We create contours that match D_s and q to the experimental data corresponding to each concentration of DECMA-1 in Fig. 1, thereby generating five contours of D_s and five of q in the $(p_0, \tilde{\eta})$ plane (Fig. 4d). The intersections between contours of

D_s and q identify the locations $(p_0, \tilde{\eta})$ in the parameter space at which the model simultaneously matches both the tissue dynamics and the tissue geometry observed in each experiment. These intersections, therefore, provide our best estimate for mapping each experimental condition onto the contour map, enabling a direct comparison between experiment and theory. The arrow in Fig. 4d indicates the trajectory through the parameter space along which tissue fluidity evolves as adhesion is systematically reduced by the DECMA-1 treatment. The results show that the dimensionless drag coefficient $\tilde{\eta}$ decreases by nearly an order of magnitude, whereas the preferred shape index p_0 remains nearly constant, ranging from 3.87 to 3.91. We note that this change in p_0 is negligible compared to the variability in the shape index between different cell monolayers (indicated by shading in Fig. 4d) and compared to the nearly order of magnitude change in $\tilde{\eta}$. Hence, changes in the dissipative contribution of adhesion dominate this fluidization process, while the interfacial adhesion energy part plays a negligible role.

Discussion

It has been widely accepted that cell shape, as quantified by the shape index, governs tissue fluidity. Our data show a striking fluidization that results from reducing cadherin-based cell-cell adhesions and is independent of shape index. Crucially, this fluidization occurs at constant density and constant cell-substrate traction. Laser ablation revealed no change in junctional line tension, indicating that the interfacial energy associated with cortical tension dominates over that of cell-cell adhesions. The original vertex model, which accounts for only the energetic effects of cell-cell adhesions and links tissue fluidity to the cell shape index, fails to explain our experimental observations. These findings indicate that cell-cell adhesions exert a second, purely dynamic effect on the collective motion: they generate forces that resist relative sliding between neighboring cells, acting as an effective viscous dissipation [30, 32–35]. We extended the original vertex model to incorporate both the energetic and dissipative contributions of cell-cell adhesion. Our extended vertex model, in which cell-cell adhesion controls two key parameters, the shape index and the viscous drag at cell-cell junctions, successfully reproduces the increase in tissue fluidity observed in the experiments.

In many prior experimental studies of tissue jamming and fluidity, changes in cell-cell adhesion occur as part of broader perturbations that simultaneously alter additional variables, such as cell motility, cortical tension, cell-substrate adhesions, or number density. In such contexts, adhesion is either a downstream consequence of a larger regulatory program or a tuning parameter whose manipulation inevitably affects multiple mechanical and dynamical properties. By contrast, in our experiments, cell-cell adhesion is perturbed while other key factors influencing tissue fluidity remain effectively constant. This design isolates adhesion as the primary control parameter and directly implicates it as a driver of tissue fluidity. Interpreted through our extended vertex model, the results offer a unifying perspective on the relationship between adhesion and tissue unjamming. This framework helps reconcile the contradictory correlations between cell-cell adhesion and tissue rigidity previously reported in the literature [7, 8, 13, 60]. This perspective is summarized in a conceptual adhesion-driven jamming phase diagram (Fig. 4e). The horizontal axis represents the energetic contribution of adhesion: increasing adhesion can elevate the preferred shape index p_0 by reducing the effective junctional line tension, thereby promoting fluidization. The vertical axis captures the dissipative contribution: decreasing adhesion reduces intercellular viscous drag, which also enhances fluidity. Because these energetic and dissipative effects act in opposition, increasing cell-cell adhesion does not lead to a universally monotonic change in tissue fluidity; instead, the net outcome depends on which contribution dominates under a given condition. An additional implication of this framework is that fluidization can occur without measurable changes in cell shape, consistent with the experimental observations reported here. A more detailed theoretical treatment of this dual and nontrivial role of adhesion is presented in the companion study [59].

The shape-independent fluidization observed here upends the prevailing geometric paradigm that tissue fluidity is defined by cell shape, which presents new directions of study based on the effects of viscous dissipation. Future theoretical efforts will be needed to bridge the macroscopic dissipative framework presented here with the microscopic kinetics of intercellular bonds. For instance, incorporating shear-dependent bond rupture or non-linear junctional remodeling could reveal how local strain rates dynamically feed back into the effective junctional viscosity. Similarly, experiments will be needed that build on recent work [35] to elucidate how viscous dissipation is related to the microstructure of the cells, including the density and location of cell-cell adhesions and the structure of the cytoskeleton. It will also be interesting to determine whether shape index and dissipation can be controlled independently, for example, by perturbing both cortical tension and cell-cell adhesion simultaneously, which could open up new opportunities for cancer treatment, tissue engineering, and wound healing.

Methods

Cell culture

MDCK type II cells expressing green fluorescent protein fused to a nuclear localization signal (a gift from Professor David Weitz, Harvard University) were cultured in Dulbecco's Modified Eagle's Medium (1 g L⁻¹ glucose, 10-014-CV, Corning) supplemented with 10% fetal bovine serum (Corning). Cells were maintained in a culture incubator (humidity maintained at 37°C with 5% CO₂) and were passaged regularly at approximately 70% confluence.

Substrate preparation and cell seeding

All experiments were carried out with cells seeded as micropatterned islands of 1 mm diameter on 75 µm-thick polyacrylamide (PA) gels with a Young's modulus of 6 kPa, using the same cell culture medium. For the kinematics and traction experiments, 0.5 µm-diameter fluorescent particles were centrifuged to the upper portion of the PA gel, as described in previous studies [36, 37]. A summary of substrate preparation and cell seeding is as follows. Glass-bottom dishes with 20 mm-diameter central wells and #1.5 bottom cover glass were used as received from Cellvis. A freshly prepared PA solution (5.5% w/v acrylamide and 0.2% w/v bisacrylamide, Biorad Laboratories) was mixed with 0.03% w/v fluorescent particles (0.5 µm-diameter, carboxylate modified, Life Technologies) as required for traction force microscopy. Ammonium persulfate (0.08% w/v, Biorad Laboratories) was added to initiate polymerization. Fifteen microliters of the gel (with or without beads) were deposited on the glass surface. Immediately after deposition, within a few minutes of polymerization, a coverslip was placed on top of the solution, and the gel was centrifuged upside down to localize the fluorescent particles near the upper portion of the gel. The final gel thickness was approximately 75 µm.

For micropatterning of 1 mm-diameter cell islands, polydimethylsiloxane (PDMS, Sylgard 184) was cured into a 200 µm-thick sheet, and holes of 1 mm diameter were punched using a biopsy punch to create a PDMS mask. The mask was sterilized with 70% ethanol and incubated in 2% w/v Pluronic F-127 (Sigma-Aldrich) overnight at room temperature. The treated PDMS mask was placed on each PA gel, which was then functionalized using sulfo-SANPAH (100 µg ml⁻¹, Pierce Biotechnology) to covalently crosslink rat-tail collagen I (Corning). One milliliter of 0.01 mg ml⁻¹ collagen solution (in autoclaved DI water) was added per gel. Dishes were covered and kept overnight at 4°C.

Cells were seeded at 1.6×10^6 ml⁻¹ and allowed to adhere for 2 h. The PDMS masks were then removed, the medium was refreshed, and cells were allowed to spread to confluence in each island over 8 h.

Maintaining constant cell density

In confined monolayers, cell density typically increases over time due to proliferation [61]. This can obscure the effects of cell-cell adhesion, as tissue fluidity, cell shape, and cellular forces depend sensitively on density [16, 19, 62]. Cell proliferation was inhibited using mitomycin C ($10 \mu\text{g ml}^{-1}$) [38], thereby maintaining a constant cell density during experiments. After reaching the desired density, the culture medium was replaced with mitomycin C-containing medium, and cells were incubated for 1 h. After that, dishes were washed twice with fresh medium and kept in the cell culture incubator with fresh medium for about 12 h prior to DECMA-1 or EGTA treatment.

DECMA-1 treatment to decrease cell-cell adhesion

To disrupt cell-cell adhesion, ten dishes containing PA gels with 1 mm cell islands were selected. The medium in each was replaced by PBS (Ca^{2+} , Mg^{2+} free standard phosphate-buffered saline) for 30 min, thereby disrupting E-cadherin-mediated cell-cell adhesions [19, 35, 39, 40]. Following this treatment, PBS was replaced with fresh culture medium supplemented with the desired concentration of the monoclonal E-cadherin antibody DECMA-1 (catalog no. 14-3249-82; research resource identifier AB-1210458; Thermo Fisher Scientific), thereby preventing the re-establishment of E-cadherin-mediated cell-cell adhesion. Note that the $0 \mu\text{g ml}^{-1}$ DECMA-1 condition is sham control, in which all procedures were performed identically, except for the addition of DECMA-1. We define the experiment time $t = 0$ h as the time of DECMA-1 addition.

Time-lapse imaging of cells and fluorescent particles

Time-lapse imaging of cell islands was started within 1.5 h of the DECMA-1 treatments. Five of the ten dishes were used for time-lapse imaging. Phase contrast images, images of green fluorescent protein (488 nm)-labeled nuclei, and images of fluorescent particles embedded in the substrate were captured every 15 min using an automated microscope (Eclipse Ti, Nikon Instruments) with a $10\times$ numerical aperture 0.3 objective (Nikon) and an Orca Flash 4.0 camera (Hamamatsu) controlled by Elements Ar software (Nikon). Cells were maintained at 37°C and 5% CO_2 using a custom-built cage incubator on the microscope stage. After imaging, the cells were detached by replacing the cell medium with 0.05% trypsin for 1 h, and images of the fluorescent particles in the substrate were captured for a traction-free reference state to compute cell-substrate tractions.

Laser ablation experiments

For laser ablation experiments, the other five dishes containing different concentrations of DECMA-1 were used. Live cells were stained for filamentous actin using the CellMaskTM Orange Actin Tracking Stain (Thermo Fisher Scientific, A57244). After 12 h incubation, laser ablations were performed on a CSU-X spinning disk confocal microscope (Yokogawa) mounted on an Eclipse Ti base with a $60\times$ NA 1.4 oil immersion objective (Nikon) and imaged with a Zyla camera (Andor), all controlled by the IQ3 acquisition software (Andor). Cell-cell edges were visualized and captured with the 561 nm laser line. A Micropoint laser (405 nm) was used to ablate cell-cell edges at 1.4 mW laser power (70% of maximum laser power, with 200 μJ maximum pulses and 10 Hz repetition rate). A confocal image was captured 1 s before the ablation as a reference; immediately after the ablation, images were acquired at 1 frame per second for 10 s.

Fixed cell imaging for E-cadherin and DECMA-1 fluorescence

The monoclonal antibody DECMA-1 binds to E-cadherin at cell-cell junctions. To verify this, cells were fixed and stained after 17 h of DECMA-1 treatment, with a cell density similar to that of the time-

lapse experiments. Cells were washed twice with PBS and fixed for 20 min with 4% w/v paraformaldehyde solution in PBS. Following fixation, cells were washed twice with PBS and permeabilized with 0.1% v/v Triton X-100 in PBS. E-cadherin was stained overnight using a E-Cadherin (24E10) Rabbit mAB Alexa Fluor 488 Conjugate (Cell Signaling 3199S; 1:250 dilution), and DECMA-1 was stained using a Goat anti-Rat IgG (H+L) Cross-Adsorbed Secondary Antibody eFluor 647 (ThermoFisher A-21247; 1:250 dilution). A Nikon AIR confocal microscope (Nikon Instruments; 40 \times -water immersion, NA 1.15) was used for imaging the samples and was controlled with NIS-Elements Ar software (Nikon). To visualize E-cadherin, and DECMA-1, a color-combined image was generated by merging color channels in Image-J to confirm the co-existence of E-cadherin and DECMA-1.

Data Analysis

Fluorescent images of nuclei were segmented with the ImageJ plugin StarDist. Then, the MALAB function ‘regionprops’ was used to get centroid positions and trajectories of nuclei for each island. Centroids and trajectories are used for further analysis, including Voronoi diagrams, number density, MSD, and average velocity.

For traction force microscopy, substrate displacements were computed by applying Fast Iterative Digital Image Correlation (FIDIC) [63] to images of the fluorescent particles using 32×32 pixel ($21 \times 21 \mu\text{m}^2$) subsets centered on a grid with spacing of 16 pixels ($10.4 \mu\text{m}$). Traction was computed with unconstrained Fourier-transform traction microscopy accounting for substrates of finite thickness [47–49].

From the laser ablation data, the velocity field v was calculated from confocal images of cells by using FIDIC using 32×32 pixel ($3.5 \times 3.5 \mu\text{m}^2$) subsets centered on a grid with spacing of 16 pixels ($1.8 \mu\text{m}$) and dividing by the imaging time (1 s). To obtain end-to-end recoil velocity (v_{IR}) or displacement (d_{IR}) along the cell edge at the ablated region, two regions of interest (ROI) were manually identified on the opposite sides of the ablated hole.

EGTA treatment to reduce cell-cell adhesion

To reduce cell-cell adhesion, the calcium chelator EGTA (Sigma-Aldrich) was applied [64] instead of DECMA-1 while keeping all other aspects of the experimental workflow unchanged. A 100 mM stock solution of EGTA was prepared in PBS. After adding EGTA to PBS, the pH was slowly increased using 40% (w/v) NaOH, as standard PBS (pH ≈ 7.4) cannot fully dissolve EGTA at 100 mM. After complete dissolution, the pH was readjusted to 7.4 using 40% (v/v) HCl. The EGTA stock solution was sterile-filtered ($0.22 \mu\text{m}$) and added to the cell culture medium at the final concentrations indicated. Here, the experiment time $t = 0$ h is the EGTA treatment time. For 0 mM EGTA islands, an equivalent amount of PBS was added as a sham treatment. Time-lapse imaging of EGTA islands was started within an hour using the same settings as discussed above.

Determination of the Uncaging Time Using Differential Dynamic Microscopy (DDM)

Differential Dynamics Microscopy (DDM) [41] is an imaging-based method that relies on time-lapse microscopy images to extract properties of system’s dynamics. DDM extracts dynamical information by analyzing temporal fluctuations in real-space images, but quantifies this information in Fourier space through the structure function $D(\mathbf{k}, \Delta t) = \langle |\Delta I(\mathbf{k}, t, \Delta t)|^2 \rangle_t$, where $I(\mathbf{k}, t, \Delta t)$ is the Fourier transform of the image difference $\Delta i(\mathbf{x}, t, \Delta t) = i(\mathbf{x}, t + \Delta t) - i(\mathbf{x}, t)$, with $i(\mathbf{x}, t)$ being the image intensity (brightness). We applied DDM to our time-lapse phase contrast images of the cell islands to extract the normalized intermediate

scattering function $F(k, \Delta t)$, which is related to azimuthal average $d(k, \Delta t)$ of the structure function [41]:

$$F(k, \Delta t) = 1 - \frac{d(k, \Delta t) - B(k)}{A(k)}. \quad (4)$$

Here, $k = |\mathbf{k}|$, $A(k)$ is the amplitude of the fluctuating signal, and $B(k)$ arises from the temporally uncorrelated detection noise. $B(k)$ is estimated as $d(k_{\max}, \Delta t \rightarrow \infty)$ with $k_{\max} = \pi/\delta_{\text{px}}$ being the upper wave vector limit that is set by the pixel size δ_{px} in our experiments. After getting $B(k)$, the signal fluctuation amplitude is estimated as $A(k) = d(k, \Delta t \rightarrow \infty) - B(k)$. To extract the cellular rearrangement time, we evaluate the scattering function at the characteristic length scale set by the crossover in the MSD. At this length scale $1/k_0 = 17 \mu\text{m}$, cell motion crosses over from independent, ballistic-like motion within a cage to diffusive-like motion governed by interactions with neighboring cells. The resultant $F_s(t)$ for different DECMA-1 concentrations show exponential decay (Supplementary Fig. 3). We define the uncaging time τ_α as the time at which the scattering function decays to $1/e$.

Estimating model units and parameters

At timescales shorter than the uncaging time τ_α , cell rearrangements are rare and cells are therefore weakly affected by interactions with their neighbors. In this regime, individual cell motion is primarily governed by single-cell motility rather than collective effects. Since the velocity persistence time also satisfies $1/D_r < 1 \text{ h} < \tau_\alpha$ [65], the polarity of each cell is uncorrelated on a timescale that is shorter than the uncaging time. Consequently, on timescales $\Delta t < \tau_\alpha$, cell motion can be well approximated by that of a self-propelled particle undergoing rotational diffusion. We thus determine the parameters v_0 and D_r by fitting the experimentally measured mean-squared displacement (MSD) at short times (specifically, for $\Delta t < 90 \text{ min}$) to the theoretical form:

$$\text{MSD}(\Delta t) = 2 \frac{v_0^2}{D_r^2} [\exp(-D_r \Delta t) + D_r \Delta t - 1]. \quad (5)$$

The experimental MSD data were fitted to the theoretical expression (Supplementary Fig. 7). The theoretical model captures the dynamics at short timescales reasonably well, allowing us to estimate v_0 and D_r as fitting parameters. The fitting results also suggest that the self-propulsion strength v_0 is minimally affected by DECMA-1 perturbation, *i.e.*, $v_0 \approx 18 \mu\text{m h}^{-1}$ for all DECMA-1 concentrations (Supplementary Fig. 7). Having obtained v_0 , we next estimate the cell-substrate viscous coefficient μ using traction measurements together with the force balance relation:

$$\mathbf{F}_i^T = \mathbf{F}_i^{\text{c-s}} + \mathbf{F}_i^{\text{act}} = \mu(v_0 \hat{\mathbf{n}}_i - \dot{\mathbf{r}}_i) \quad (6)$$

Where \mathbf{F}_i^T is the traction force exerted by the substrate on cell i . To compute \mathbf{F}_i^T for each cell, we first extract the traction field defined on spatial grids over the cell island. We then perform a Voronoi tessellation using the cell nucleus positions to approximate individual cell domains. The traction acting on a given cell is obtained by vector summing the traction forces over all grid points that are mapped to the corresponding Voronoi region. Starting from Eq. 6, we can eliminate the (unobserved) polarity vector $\hat{\mathbf{n}}_i$ by taking the norm of both sides, which yields $\|\mathbf{F}_i^T + \mu \dot{\mathbf{r}}_i\| = \mu v_0$. This relation connects the measurable quantities v_0 , \mathbf{F}_i^T and $\dot{\mathbf{r}}_i$ to the unknown parameter μ . We estimate the cell-substrate viscous coefficient μ by fitting this relation to the data. Specifically, we choose μ to minimize the residual $R(\mu) = \sum_i (\|\mathbf{F}_i^T + \mu \dot{\mathbf{r}}_i\| - \mu v_0)^2$. We determine μ from the $0 \mu\text{g ml}^{-1}$ DECMA-1 condition and use this value for all other DECMA-1 concentrations, assuming that DECMA-1 does not significantly affect cell-substrate interactions, as indicated by the weak dependence of v_0 on DECMA-1 concentration. All simulations use $A_0/\bar{A} = 1$. The parameter K_A is obtained from the areal strain modulus $\kappa_A = 0.05 \text{ N m}^{-1}$ for MDCK II cells, which was estimated using Atomic Force

Microscopy (AFM) [66], as $K_A = \kappa_A/\bar{A} \approx 0.11 \text{ N m}^{-3}$. Using these estimated parameters, we express our experimental results in units of length $l_0 = \sqrt{\bar{A}} \approx 20 \text{ }\mu\text{m}$ and time $t_0 = \mu/(K_A\bar{A}) \approx 0.0055 \text{ h}$.

In these length and time units, a value of $v_0 \approx 18 \text{ }\mu\text{m h}^{-1}$ corresponds to a dimensionless $\tilde{v}_0 = 0.0027$, which is practically 0 for our simulation, making the dynamics difficult to be describe in a reasonable simulation time. Exploiting the proportionality between the self-diffusivity D_s and the persistence length $L_p = v_0/D_r \approx 0.3l_0$, we run simulations at larger \tilde{v}_0 and \tilde{D}_r while keeping their ratio fixed to match the experimental persistence length. Specifically, we choose $\tilde{v}_0 = 0.3$ and $\tilde{D}_r = 1$, which preserves the single-cell persistence length $\tilde{L}_p = 0.3$ while accelerating convergence to the long-time diffusive regime. Importantly, this choice of motility parameters does not affect our central conclusion regarding the dominant role of dissipative adhesion. While increasing \tilde{v}_0 enhances fluidity, its effect can be offset by a corresponding increase in the viscous drag cell-cell adhesion $\tilde{\eta}$, which is equivalent to a vertical shift in the $p_0 - \tilde{\eta}$ plane. Such a shift leaves the direction and qualitative trend of the fluidization trajectory unchanged. We therefore expect the dominance of dissipative adhesion to be robust to the specific choice of \tilde{v}_0 and \tilde{D}_r , provided L_p is held fixed. To generate the contours of constant D_s and constant q , we systematically sweep the parameter space by varying p_0 from 3.72 to 3.99 and $\tilde{\eta}$ from 0.01 to 100, while keeping $\tilde{K}_P = K_P/(K_A\bar{A})$ fixed at a value of 1. For each parameter pair $(p_0, \tilde{\eta})$, we simulate the tissue dynamics by numerically integrating Eq. 3 using an explicit Euler scheme with time step $dt = 0.05$, and we evolve the system until a total simulation time of 10^4 is reached, ensuring that steady-state behavior is attained.

Statistics and reproducibility

The experiments tested the response to a range of concentrations of DECMA-1 or EGTA. For these experiments, statistical tests using categorical independent variables, such as ANOVA, do not accurately capture the effect of concentration, which is a continuous variable. Therefore, for each data set, we began with a linear correlation, and acquired the p value against the null hypothesis of no correlation, with statistical significance defined as $p < 0.05$. For all cases in which the correlation returned $p > 0.05$, we performed a more detailed investigation, using one-way ANOVA with Dunnett’s test, which compared the data from each concentration of DECMA-1 or EGTA to the sham control. p values from the Dunnett’s test are included in the supplementary information.

The time-lapse imaging and laser ablation experiments involving DECMA-1 and EGTA treatments were repeated multiple times to assess reproducibility. All groups were subjected to identical culture, treatment, and imaging protocols to control for potential covariates, thereby ensuring comparability across conditions. The results shown in the manuscript are representative of the multiple different experiments. Importantly, the observed trends were consistent across all repeated experiments.

The custom code developed for the simulation in this study is available at GitHub Repository (<https://github.com/nqanh1995/Vertex-model-with-viscous-adhesion>) under the MIT license.

References

- [1] Friedl, P. & Gilmour, D. Collective cell migration in morphogenesis, regeneration and cancer. *Nature reviews molecular cell biology* **10**, 445–457 (2009). URL <https://www.nature.com/articles/nrm2720>.
- [2] Sadati, M., Qazvini, N. T., Krishnan, R., Park, C. Y. & Fredberg, J. J. Collective migration and cell jamming. *Differentiation* **86**, 121–125 (2013). URL <https://www.sciencedirect.com/science/article/pii/S0301468113000170?via%3Dihub>.

- [3] Frittoli, E. *et al.* Tissue fluidification promotes a cgas–sting cytosolic dna response in invasive breast cancer. *Nature materials* **22**, 644–655 (2023). URL <https://www.nature.com/articles/s41563-022-01431-x>.
- [4] Zitong, C., Zhenyu, C. & Rinkevich, Y. Tissue fluidity: biophysical shape-shifting for regeneration. *Signal Transduction and Targeted Therapy* **9**, 329 (2024). URL <https://www.nature.com/articles/s41392-024-02068-9>.
- [5] Herrera-Perez, R. M. & Kasza, K. E. Biophysical control of the cell rearrangements and cell shape changes that build epithelial tissues. *Current opinion in genetics & development* **51**, 88–95 (2018). URL <https://www.sciencedirect.com/science/article/pii/S0959437X1730117X?via%3Dihub>.
- [6] Wang, X. *et al.* Anisotropy links cell shapes to tissue flow during convergent extension. *Proceedings of the National Academy of Sciences* **117**, 13541–13551 (2020). URL <https://www.pnas.org/doi/10.1073/pnas.1916418117>.
- [7] Cai, G. *et al.* Compressive stress drives adhesion-dependent unjamming transitions in breast cancer cell migration. *Frontiers in Cell and Developmental Biology* **10**, 933042 (2022). URL <https://www.frontiersin.org/journals/cell-and-developmental-biology/articles/10.3389/fcell.2022.933042/full>.
- [8] Tetley, R. J. *et al.* Tissue fluidity promotes epithelial wound healing. *Nature physics* **15**, 1195–1203 (2019). URL <https://www.nature.com/articles/s41567-019-0618-1>.
- [9] Sarate, R. M. *et al.* Dynamic regulation of tissue fluidity controls skin repair during wound healing. *Cell* **187**, 5298–5315 (2024). URL <https://www.sciencedirect.com/science/article/pii/S0092867424008250?via%3Dihub>.
- [10] Bi, D., Lopez, J., Schwarz, J. M. & Manning, M. L. A density-independent rigidity transition in biological tissues. *Nature Physics* **11**, 1074–1079 (2015). URL <https://www.nature.com/articles/nphys3471>.
- [11] Sahu, P., Kang, J., Erdemci-Tandogan, G. & Manning, M. L. Linear and nonlinear mechanical responses can be quite different in models for biological tissues. *Soft Matter* **16**, 1850–1856 (2020). URL <https://pubs.rsc.org/en/content/articlelanding/2020/sm/c9sm01068h>.
- [12] Bi, D., Lopez, J. H., Schwarz, J. M. & Manning, M. L. Energy barriers and cell migration in densely packed tissues. *Soft matter* **10**, 1885–1890 (2014).
- [13] Park, J.-A. *et al.* Unjamming and cell shape in the asthmatic airway epithelium. *Nature materials* **14**, 1040–1048 (2015). URL <https://www.nature.com/articles/nmat4357>.
- [14] Malinverno, C. *et al.* Endocytic reawakening of motility in jammed epithelia. *Nature materials* **16**, 587–596 (2017).
- [15] Mongera, A. *et al.* A fluid-to-solid jamming transition underlies vertebrate body axis elongation. *Nature* **561**, 401–405 (2018). URL <https://www.nature.com/articles/s41586-018-0479-2>.
- [16] Saraswathibhatla, A. & Notbohm, J. Traction and stress fibers control cell shape and rearrangements in collective cell migration. *Phys. Rev. X* **10**, 011016 (2020). URL <https://journals.aps.org/prx/abstract/10.1103/PhysRevX.10.011016>.

- [17] Mitchel, J. A. *et al.* In primary airway epithelial cells, the unjamming transition is distinct from the epithelial-to-mesenchymal transition. *Nature communications* **11**, 5053 (2020).
- [18] Wang, X., Cupo, C. M., Ostvar, S., Countryman, A. D. & Kasza, K. E. E-cadherin tunes tissue mechanical behavior before and during morphogenetic tissue flows. *Current Biology* **34**, 3367–3379 (2024). URL <https://www.sciencedirect.com/science/article/pii/S0960982224008224>.
- [19] Chisolm, S. J., Guo, E., Subramaniam, V., Schulze, K. D. & Angelini, T. E. Transitions between cooperative and crowding-dominated collective motion in non-jammed mdck monolayers. *Cells & Development* **181**, 203989 (2025). URL <https://www.sciencedirect.com/science/article/pii/S2667290124000998?via%3Dihub>.
- [20] Nagai, T. & Honda, H. A dynamic cell model for the formation of epithelial tissues. *Philosophical Magazine B* **81**, 699–719 (2001).
- [21] Farhadifar, R., Röper, J.-C., Aigouy, B., Eaton, S. & Jülicher, F. The influence of cell mechanics, cell-cell interactions, and proliferation on epithelial packing. *Current biology* **17**, 2095–2104 (2007). URL <https://www.sciencedirect.com/science/article/pii/S0960982207023342?via%3Dihub>.
- [22] Hufnagel, L., Teleman, A. A., Rouault, H., Cohen, S. M. & Shraiman, B. I. On the mechanism of wing size determination in fly development. *Proceedings of the National Academy of Sciences* **104**, 3835–3840 (2007).
- [23] Chiou, K. K., Hufnagel, L. & Shraiman, B. I. Mechanical stress inference for two dimensional cell arrays. *PLoS computational biology* **8**, e1002512 (2012).
- [24] Brodland, G. W. The differential interfacial tension hypothesis (dith): a comprehensive theory for the self-rearrangement of embryonic cells and tissues. *J Biomech Eng* **124**, 188–197 (2002). URL <https://asmedigitalcollection.asme.org/biomechanical/article/124/2/188/416919>.
- [25] Lecuit, T. & Lenne, P.-F. Cell surface mechanics and the control of cell shape, tissue patterns and morphogenesis. *Nature reviews Molecular cell biology* **8**, 633–644 (2007). URL <https://www.nature.com/articles/nrm2222>.
- [26] Hilgenfeldt, S., Erisken, S. & Carthew, R. W. Physical modeling of cell geometric order in an epithelial tissue. *Proceedings of the National Academy of Sciences* **105**, 907–911 (2008). URL <https://www.pnas.org/doi/full/10.1073/pnas.0711077105>.
- [27] Paluch, E. & Heisenberg, C.-P. Biology and physics of cell shape changes in development. *Current Biology* **19**, R790–R799 (2009). URL [https://www.cell.com/current-biology/fulltext/S0960-9822\(09\)01451-1](https://www.cell.com/current-biology/fulltext/S0960-9822(09)01451-1).
- [28] Manning, M. L., Foty, R. A., Steinberg, M. S. & Schoetz, E.-M. Coaction of intercellular adhesion and cortical tension specifies tissue surface tension. *Proceedings of the National Academy of Sciences* **107**, 12517–12522 (2010). URL <https://www.pnas.org/doi/10.1073/pnas.1003743107>.
- [29] Winklbauer, R. Cell adhesion strength from cortical tension—an integration of concepts. *Journal of cell science* **128**, 3687–3693 (2015). URL <https://journals.biologists.com/jcs/article/128/20/3687/55263/Cell-adhesion-strength-from-cortical-tension-an>.

- [30] Lenne, P.-F., Rupprecht, J.-F. & Viasnoff, V. Cell junction mechanics beyond the bounds of adhesion and tension. *Developmental Cell* **56**, 202–212 (2021). URL https://www.sciencedirect.com/science/article/pii/S1534580720310248?utm_source.
- [31] Herrera-Perez, R. M., Cupo, C., Allan, C., Dagle, A. B. & Kasza, K. E. Tissue flows are tuned by actomyosin-dependent mechanics in developing embryos. *PRX Life* **1**, 013004 (2023). URL <https://link.aps.org/doi/10.1103/PRXLife.1.013004>.
- [32] Fu, C. *et al.* Regulation of intercellular viscosity by e-cadherin-dependent phosphorylation of EGFR in collective cell migration. *Proceedings of the National Academy of Sciences* **121**, e2405560121 (2024). URL <https://www.pnas.org/doi/full/10.1073/pnas.2405560121>.
- [33] Arora, A. *et al.* Viscous dissipation in the rupture of cell–cell contacts. *Nature Materials* 1–11 (2025). URL <https://www.nature.com/articles/s41563-025-02232-8>.
- [34] McCord, M. & Notbohm, J. Energy injection in an epithelial cell monolayer indicated by negative viscosity. *PRX Life* **3**, 043017 (2025). URL <https://journals.aps.org/prxlife/abstract/10.1103/91nm-gm3j>.
- [35] McCord, M. & Notbohm, J. Measurement of tissue viscosity to relate force and motion in collective cell migration. *Soft matter* **22**, 458–473 (2026). URL <https://pubs.rsc.org/en/content/articlelanding/2026/sm/d5sm01139f>.
- [36] Notbohm, J. *et al.* Cellular contraction and polarization drive collective cellular motion. *Biophys. J.* **110**, 2729–2738 (2016). URL <https://www.sciencedirect.com/science/article/pii/S0006349516303010?via%3Dihub>.
- [37] Bera, P. K., McCord, M., Zhang, J. & Notbohm, J. Traction and stress control formation and motion of $1/2$ topological defects in epithelial cell monolayers. *Newton* **1** (2025). URL [https://www.cell.com/newton/fulltext/S2950-6360\(25\)00223-3](https://www.cell.com/newton/fulltext/S2950-6360(25)00223-3).
- [38] Jain, S. *et al.* The role of single-cell mechanical behaviour and polarity in driving collective cell migration. *Nature physics* **16**, 802–809 (2020). URL <https://www.nature.com/articles/s41567-020-0875-z>.
- [39] Noren, N. K., Niessen, C. M., Gumbiner, B. M. & Burridge, K. Cadherin engagement regulates rho family gtpases. *Journal of Biological Chemistry* **276**, 33305–33308 (2001). URL [https://www.jbc.org/article/S0021-9258\(19\)34714-3/fulltext](https://www.jbc.org/article/S0021-9258(19)34714-3/fulltext).
- [40] Shim, G., Devenport, D. & Cohen, D. J. Overriding native cell coordination enhances external programming of collective cell migration. *Proceedings of the National Academy of Sciences* **118**, e2101352118 (2021). URL <https://www.pnas.org/doi/full/10.1073/pnas.2101352118>.
- [41] Lattuada, E., Krautgasser, F., Lavaud, M., Giavazzi, F. & Cerbino, R. The hitchhiker’s guide to differential dynamic microscopy. *The Journal of Chemical Physics* **163** (2025). URL <https://pubs.aip.org/aip/jcp/article/163/16/161501/3369109/The-Hitchhiker-s-guide-to-differential-dynamic>.
- [42] Bi, D., Yang, X., Marchetti, M. C. & Manning, M. L. Motility-driven glass and jamming transitions in biological tissues. *Phys. Rev. X* **6**, 021011 (2016). URL <https://journals.aps.org/prx/abstract/10.1103/PhysRevX.6.021011>.

- [43] Eckert, J., Ladoux, B., Mège, R.-M., Giomi, L. & Schmidt, T. Hexanematic crossover in epithelial monolayers depends on cell adhesion and cell density. *Nature Communications* **14**, 5762 (2023). URL <https://www.nature.com/articles/s41467-023-41449-6>.
- [44] Kusaka, E. M. *et al.* Cell rearrangement progression along the apical-basal axis is linked with 3d epithelial tissue structure. *PRX Life* **4**, 013005 (2026). URL <https://journals.aps.org/prxlife/abstract/10.1103/15r5-pb9t>.
- [45] Krieg, M. *et al.* Tensile forces govern germ-layer organization in zebrafish. *Nature cell biology* **10**, 429–436 (2008). URL <https://www.nature.com/articles/ncb1705>.
- [46] Maître, J.-L. *et al.* Adhesion functions in cell sorting by mechanically coupling the cortices of adhering cells. *science* **338**, 253–256 (2012). URL <https://www.science.org/doi/10.1126/science.1225399>.
- [47] Butler, J. P., Tolic-Nørrelykke, I. M., Fabry, B. & Fredberg, J. J. Traction fields, moments, and strain energy that cells exert on their surroundings. *Am. J. Physiol. Cell Physiol.* **282**, C595–C605 (2002). URL <https://journals.physiology.org/doi/full/10.1152/ajpcell.00270.2001>.
- [48] Del Alamo, J. C. *et al.* Spatio-temporal analysis of eukaryotic cell motility by improved force cytometry. *P. Natl. Acad. Sci. USA* **104**, 13343–13348 (2007). URL <https://www.pnas.org/doi/full/10.1073/pnas.0705815104>.
- [49] Trepap, X. *et al.* Physical forces during collective cell migration. *Nat. Phys.* **5**, 426–430 (2009). URL <https://www.nature.com/articles/nphys1269>.
- [50] Shapiro, L. & Weis, W. I. Structure and biochemistry of cadherins and catenins. *Cold Spring Harbor perspectives in biology* **1**, a003053 (2009). URL <https://cshperspectives.cshlp.org/content/1/3/a003053.short>.
- [51] Moazzeni, S. *et al.* N-cadherin based adhesion and rac1 activity regulate tension polarization in the actin cortex. *Scientific reports* **15**, 4296 (2025). URL <https://www.nature.com/articles/s41598-025-88537-9>.
- [52] Maître, J.-L. & Heisenberg, C.-P. The role of adhesion energy in controlling cell–cell contacts. *Current opinion in cell biology* **23**, 508–514 (2011). URL <https://www.sciencedirect.com/science/article/pii/S0955067411000871>.
- [53] Sussman, D. M. & Merkel, M. No unjamming transition in a voronoi model of biological tissue. *Soft matter* **14**, 3397–3403 (2018). URL <https://pubs.rsc.org/en/content/articlehtml/2018/sm/c7sm02127e>.
- [54] Sussman, D. M. Interplay of curvature and rigidity in shape-based models of confluent tissue. *Physical Review Research* **2**, 023417 (2020). URL <https://journals.aps.org/prresearch/abstract/10.1103/PhysRevResearch.2.023417>.
- [55] Nguyen, A. Q., Huang, J. & Bi, D. Origin of yield stress and mechanical plasticity in model biological tissues. *Nature Communications* **16**, 3260 (2025). URL <https://www.nature.com/articles/s41467-025-58526-7>.
- [56] Ansell, H. S., Li, C. & Sussman, D. M. Tunable glassy dynamics in models of dense cellular tissue. *Physical Review E* **112**, L013403 (2025). URL <https://journals.aps.org/pre/abstract/10.1103/ryy4-2xt6>.

- [57] Tong, S., Sknepnek, R. & Košmrlj, A. Linear viscoelastic response of the vertex model with internal and external dissipation: Normal modes analysis. *Physical Review Research* **5**, 013143 (2023). URL <https://journals.aps.org/prresearch/abstract/10.1103/PhysRevResearch.5.013143>.
- [58] Rozman, J., Chaithanya, K., Yeomans, J. M. & Sknepnek, R. Vertex model with internal dissipation enables sustained flows. *Nature Communications* **16**, 530 (2025). URL <https://www.nature.com/articles/s41467-025-55820-2>.
- [59] Nguyen, A. Q., Bera, P. K., Notbohm, J. & Bi, D. Cell-cell adhesion as a double-edged sword in tissue fluidity (2026). Manuscript in preparation.
- [60] Garcia, S. *et al.* Physics of active jamming during collective cellular motion in a monolayer. *Proceedings of the National Academy of Sciences* **112**, 15314–15319 (2015).
- [61] Bocanegra-Moreno, L., Singh, A., Hannezo, E., Zagorski, M. & Kicheva, A. Cell cycle dynamics control fluidity of the developing mouse neuroepithelium. *Nature Physics* **19**, 1050–1058 (2023). URL <https://www.nature.com/articles/s41567-023-01977-w>.
- [62] Kocgozlu, L. *et al.* Epithelial cell packing induces distinct modes of cell extrusions. *Current Biology* **26**, 2942–2950 (2016). URL <https://www.sciencedirect.com/science/article/pii/S0960982216310028?via%3Dihub>.
- [63] Bar-Kochba, E., Toyjanova, J., Andrews, E., Kim, K.-S. & Franck, C. A fast iterative digital volume correlation algorithm for large deformations. *Exp. Mech.* **55**, 261–274 (2015). URL <https://link.springer.com/article/10.1007/s11340-014-9874-2>.
- [64] Saraswathibhatla, A., Zhang, J. & Notbohm, J. Coordination of contractile tension and cell area changes in an epithelial cell monolayer. *Physical Review E* **105**, 024404 (2022). URL <https://journals.aps.org/pre/abstract/10.1103/PhysRevE.105.024404>.
- [65] Saraswathibhatla, A., Henkes, S., Galles, E. E., Sknepnek, R. & Notbohm, J. Coordinated tractions increase the size of a collectively moving pack in a cell monolayer. *Extreme Mech. Lett.* **48**, 101438 (2021). URL <https://www.sciencedirect.com/science/article/pii/S2352431621001589?via%3Dihub>.
- [66] Bodenschatz, J. F. *et al.* Epithelial cells sacrifice excess area to preserve fluidity in response to external mechanical stress. *Communications Biology* **5**, 855 (2022). URL <https://www.nature.com/articles/s42003-022-03809-8>.

Acknowledgments

We thank Christian Franck for the use of the A1R confocal microscope. J.N. acknowledges support from NSF Grant No. CMMI-2205141 and NIH Grant No. R35GM151171. A.N. and D.B. acknowledge support from NSF Grants No. DMR-2046683 and PHY-2019745, the Sloan Research Fellowship, NIH Grant No. R35GM150494 and the Human Frontier Science Program research grant (RGP0007/2022).

Author Contributions

P.K.B. performed the experiments and data analysis under the supervision of J.N. A.Q.N. performed the simulations under the supervision of D.B. M.M. performed fixed-cell confocal imaging. P.K.B., A.Q.N., D.B., and J.N. conceived the study, interpreted the results, and wrote the manuscript.

Competing interests

The authors declare no competing interests.

Additional information

Supplementary information is available for this paper and includes Supplementary Figures and Supplementary Tables. Correspondence and requests for materials should be addressed to Pradip K. Bera or Jacob Notbohm.

Supplementary Information

Shape-Independent Fluidization in Epithelial Cell Monolayers

Pradip K. Bera¹, Anh Q. Nguyen^{2,3}, Molly McCord^{1,4}, Dapeng Bi^{2,3}, Jacob Notbohm^{1,4,†}

¹ Department of Mechanical Engineering, University of Wisconsin–Madison, Madison, WI, USA

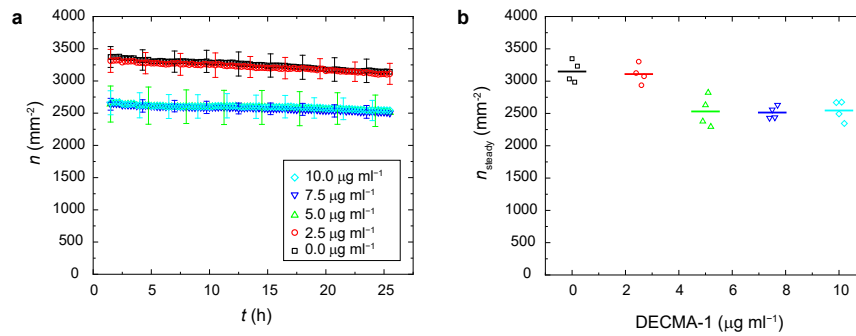
² Department of Physics, Northeastern University, Boston, MA, USA

³ Center for Theoretical Biological Physics, Northeastern University, Boston, MA, USA

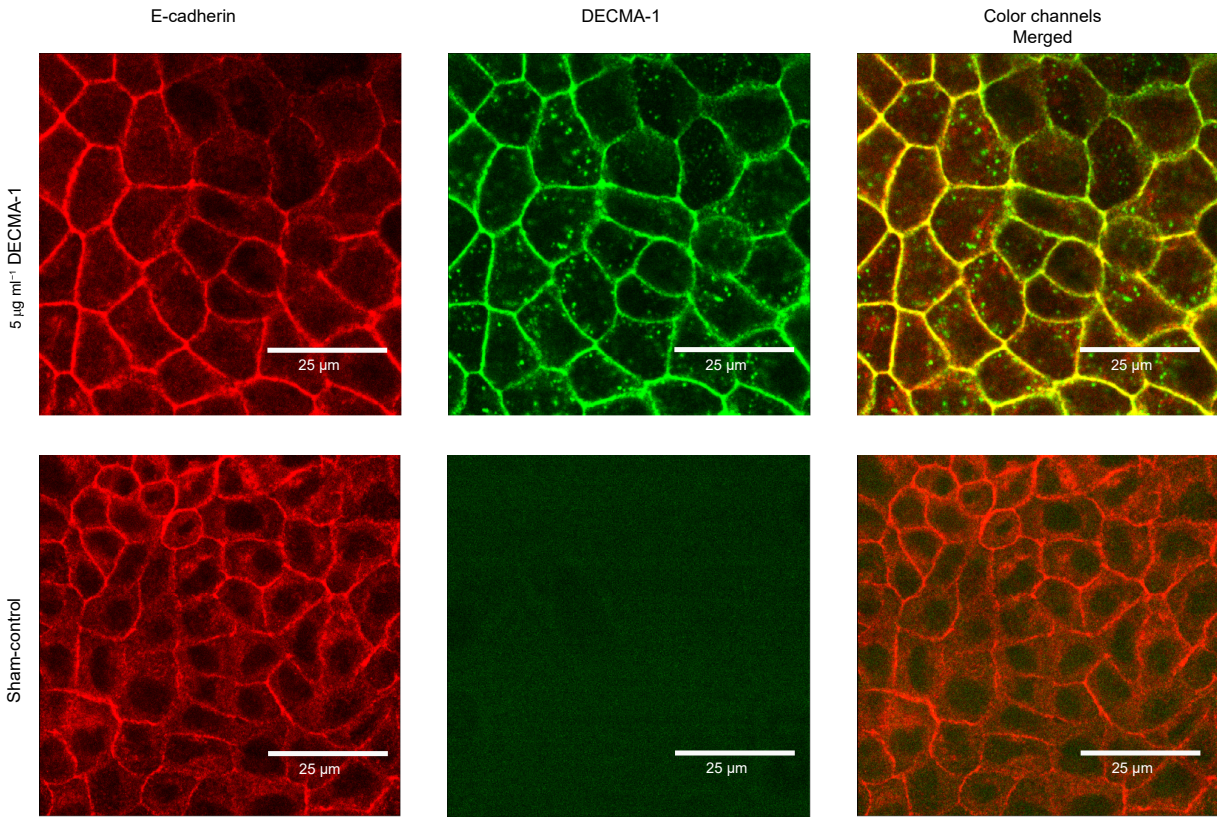
⁴ Biophysics Program, University of Wisconsin–Madison, Madison, WI, USA

† Correspondence: jknotbohm@wisc.edu

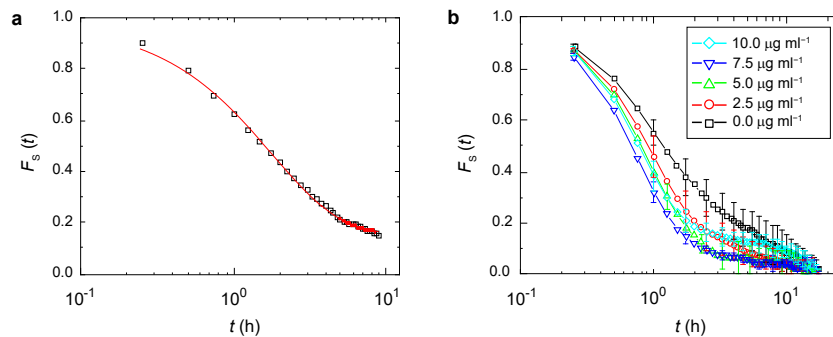
Supplementary Figures



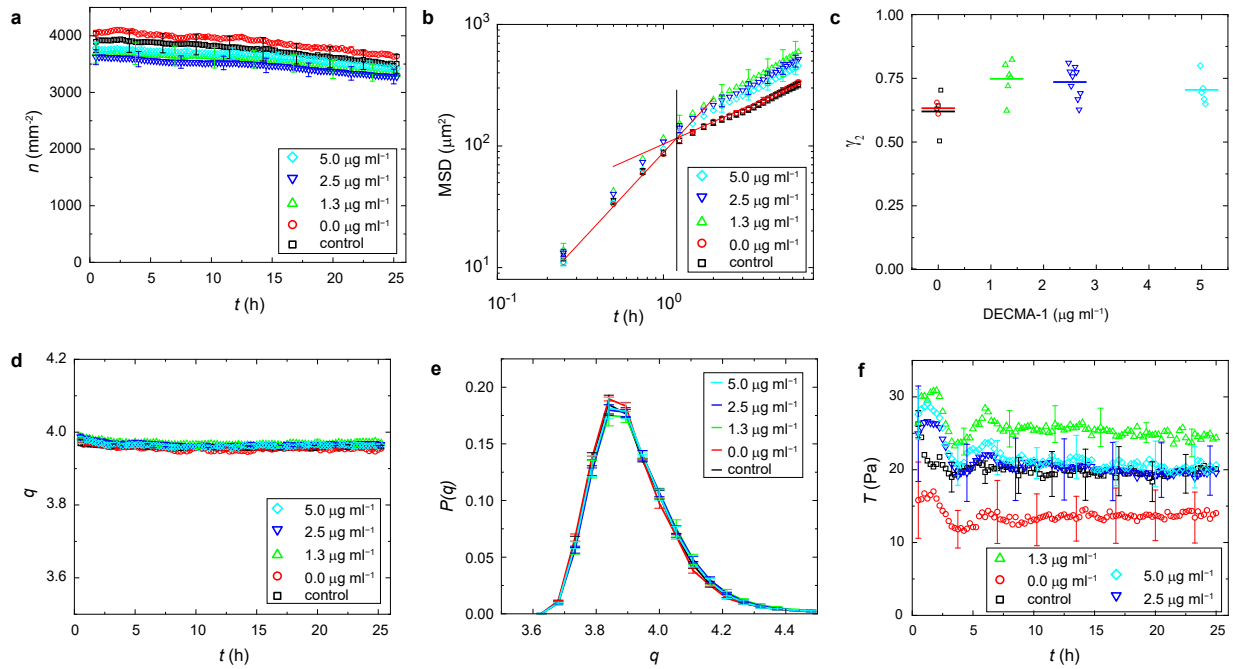
Supplementary Fig. 1: Number density during the DECMA-1 experiment (Fig. 1). Number density was computed at each frame by counting nuclei within each island and dividing by island area. (a) Average number density n for each DECMA-1 concentration, with error bars indicating standard deviations across different cell monolayers. (b) Plotted n_{steady} , the steady state density defined as the average over $t = 23\text{--}24$ h ($p = 5.8 \times 10^{-5}$). Horizontal lines denote means of respective groups. Although the number density was statistically different across the different DECMA-1 concentrations, the relative values are in a small range of $\approx 2500\text{--}3200$ mm⁻². Prior studies that have shown effects of density on collective migration [main text Ref. [16]] have used a much larger range, *e.g.*, 1200–4200 mm⁻¹, meaning that any effects of the small range of density in these experiments are likely to be modest. Furthermore, additional experimental data in this manuscript (Fig. 3 and Supplementary Fig. 4) show no correlation between density and kinematics, which rules out density as the cause of the fluidization reported here.



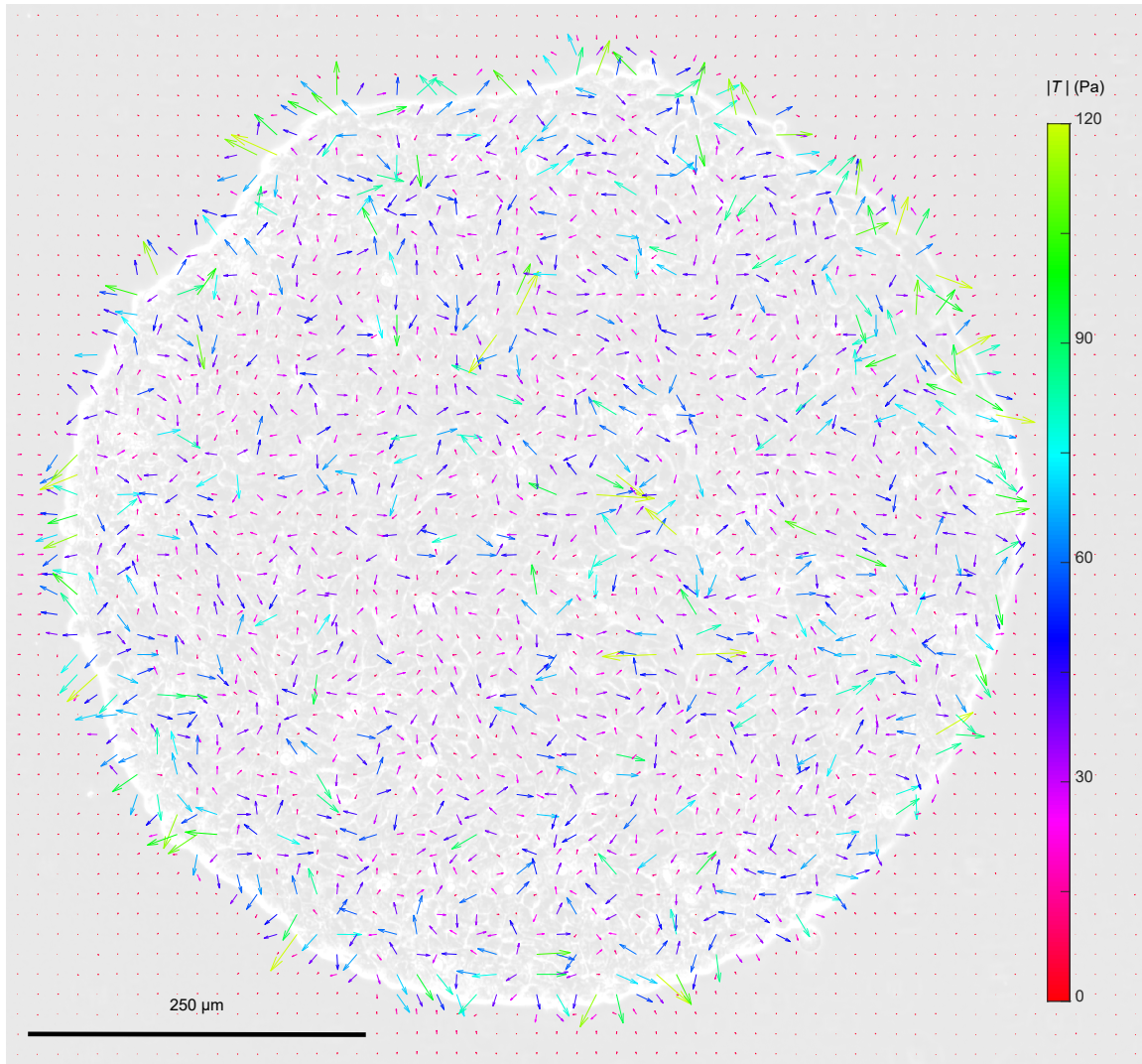
Supplementary Fig. 2: Verification that DECMA-1 binds to E-cadherin. Top row, left to right: Confocal images of E-cadherin (red) and DECMA-1 (green) in cells fixed after 17 h, for a represented region in a cell monolayer treated with $5 \mu\text{g ml}^{-1}$ DECMA-1; merging color channels appears yellow, indicating co-localization of E-cadherin and DECMA-1, which verifies that DECMA-1 bound to E-cadherin. Bottom row, left to right: similar plots for $0 \mu\text{g ml}^{-1}$ show no green fluorescence, indicating that the antibody used for imaging DECMA-1 bound specifically to DECMA-1 in the $5 \mu\text{g ml}^{-1}$ condition.



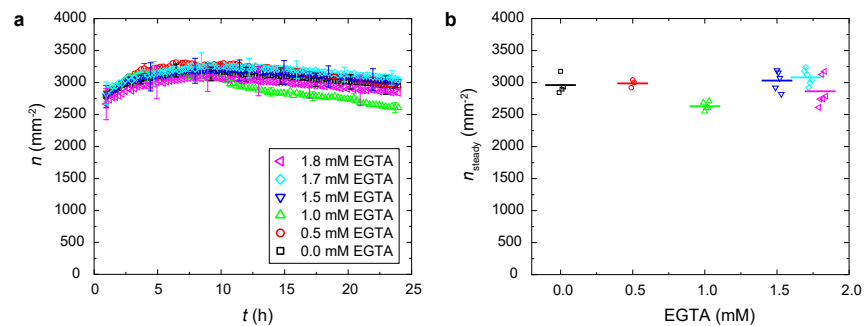
Supplementary Fig. 3: Self-intermediate scattering function for different concentrations of DECMA-1. (a) For a representative $0 \mu\text{g ml}^{-1}$ DECMA-1 island, the self-intermediate scattering function F_s is plotted in time; the red curve is an exponential fit. (b) F_s is plotted for all the DECMA-1 concentrations. F_s decays more rapidly at higher DECMA-1 concentrations, indicating smaller τ_α . Markers and error bars respectively, indicate averages and standard deviations across different independent cell islands.



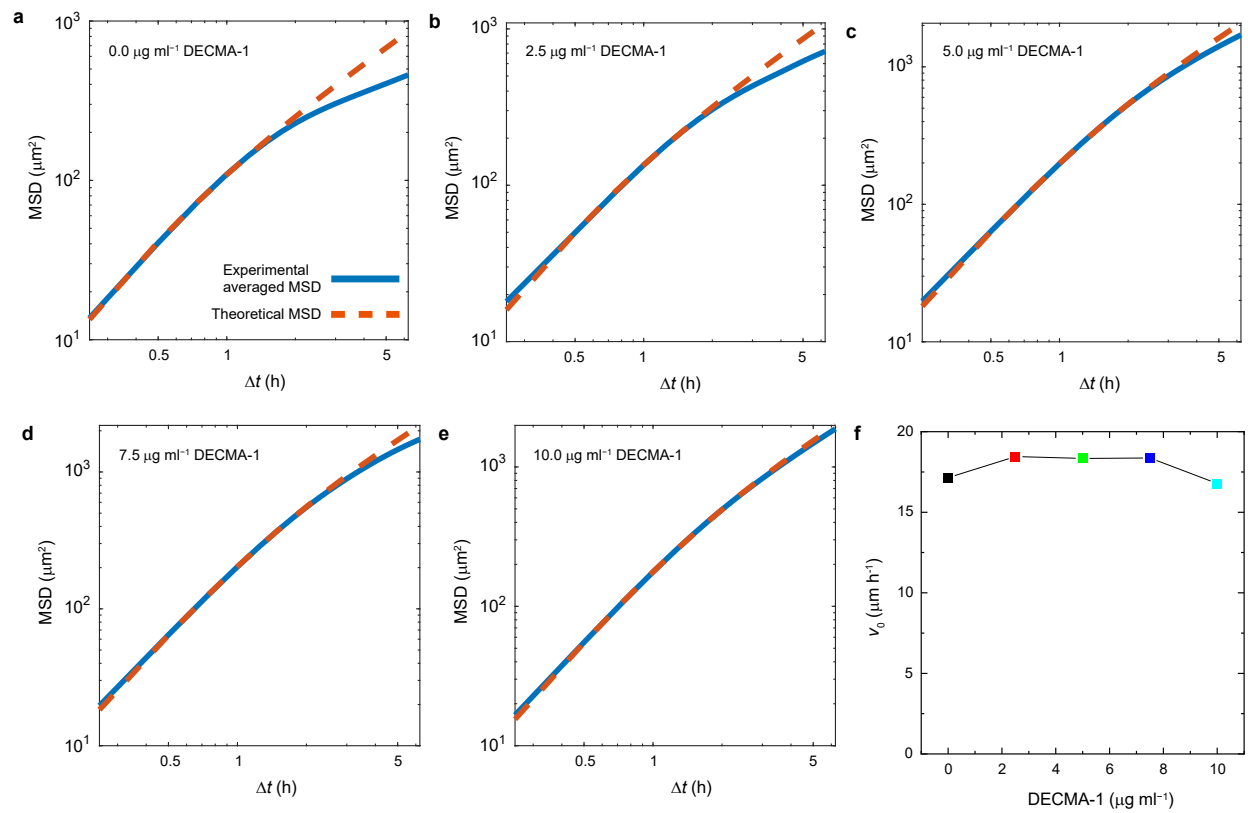
Supplementary Fig. 4: Effects of DECMA-1 on kinematics and forces in cell islands at higher cell density ($3500 < n < 4500 \text{ mm}^{-2}$). Control monolayers had no PBS added, and the $0 \mu\text{g ml}^{-1}$ concentration of DECMA-1 is a sham control, wherein PBS was added followed by replacing the PBS with cell culture medium containing no DECMA-1. Plots for: (a) number density n , (b) mean-squared displacement (MSD), (c) the long-time MSD exponent γ_2 ($p = 0.21$; extended statistical test in Supplementary Table 4), (d) cell shape index q , (e) steady-state distributions of q considering time interval $t = 23-24$ h, and (f) traction T . Error bars are standard deviations. Horizontal lines denote means of respective groups.



Supplementary Fig. 5: Representative two-dimensional traction vector field (corresponding to Fig. 1a in the main text). Vectors are spatially downsampled by a factor of two for clarity, color-coded by traction magnitude, and overlaid on a semi-transparent monolayer image to enhance visualization. Small arrows at grid points far from the island indicate the traction noise level. A scale bar is included.



Supplementary Fig. 6: Number density in EGTA experiment. (a) Number density n plotted in time. (b) n_{steady} steady state density, defined as the average over $t = 22\text{--}23$ h ($p = 0.58$; extended statistical test in Supplementary Table 2).



Supplementary Fig. 7: MSD of cells at different adhesion levels (DECMA-1 concentrations) are fitted to the theoretical MSD of self-propelled particles undergoing rotational diffusion (main text Eq. 5). Fits are shown separately in panels (a-e) for all DECMA-1 concentrations. (f) Extracted self-propulsion strength v_0 plotted against DECMA-1 concentration.

Supplementary Tables

Supplementary Table 1: Extended statistical analysis of results in Fig. 2 (DECMA-1 treatment) using one-way ANOVA with Dunnett's test. All p values are with respect to sham control ($0 \mu\text{g ml}^{-1}$).

DECMA-1 ($\mu\text{g ml}^{-1}$)	v_{IR} p -value	T_{steady} p -value
2.5	0.045	1.0
5	0.66	0.96
7.5	0.67	0.95
10	0.96	0.73

Supplementary Table 2: Extended statistical analysis of results in Fig. 3 (EGTA treatment) using one-way ANOVA with Dunnett's test. All p values are with respect to sham control (0 mM).

EGTA (mM)	q_{steady} p -value	v_{IR} p -value	n_{steady} p -value
0.5	1.0	0.020	1.0
1	0.99	0.040	0.014
1.5	1.0	0.95	0.92
1.7	0.46	0.31	0.60
1.8	0.36	0.37	0.76

Supplementary Table 3: Model parameters that best match the experiments. These parameters correspond to the stars in Fig. 4d. The dimensionless quantities can be computed using the unit of time as $t_0 = \mu / (K_A \bar{A})$, the unit of length as $l_0 = \sqrt{\bar{A}}$, and the unit of force as $K_A \bar{A}^{3/2}$. As described in the main text, the dimensionless viscous drag is given by $\tilde{\eta} = \eta \sqrt{\bar{A}} / \mu$.

DECMA-1 concentration ($\mu\text{g ml}^{-1}$)	cell-substrate viscous coefficient μ (nN.h μm^{-1})	area elasticity K_A (nN μm^{-3})	average cell area \bar{A} (μm^2)	preferred shape index p_0	junctional drag coefficient η (nN.h μm^{-2})
0	0.247	0.11	349	3.88	0.126
2.5	0.247	0.11	391	3.89	0.083
5	0.247	0.11	434	3.91	0.048
7.5	0.247	0.11	430	3.91	0.043
10	0.247	0.11	433	3.90	0.027

Supplementary Table 4: Extended statistical analysis of results from the DECMA-1 experiment at higher cell density shown in Supplementary Fig. 4 using one-way ANOVA with Dunnett's test. All p values are in comparison to sham control ($0 \mu\text{g ml}^{-1}$ DECMA-1).

DECMA-1 ($\mu\text{g ml}^{-1}$)	γ_2 p -value
1.3	7.2×10^{-9}
2.5	5.4×10^{-9}
5	2.3×10^{-8}